Stimuli responsive micro-architected materials

Thesis by

Luizetta Vadimovna Elliott

In Partial Fulfillment of the Requirements for

the degree of

Doctor of Philosophy

Caltech

CALIFORNIA INSTITUTE OF TECHNOLOGY

Pasadena, California

2021

(Defended December 18, 2020)

© 2021

Luizetta Vadimovna Elliott
ORCID: 0000-0002-6411-0239

ACKNOWLEDGEMENTS

ABSTRACT

Shape memory polymers (SMPs) respond to heat by generating programmable movement useful in devices that require substantial deformation and operate at transient temperatures, including stents, embolization coils, and robotic grippers. Transitioning these materials to the microscale can result in expanded potential applications, such as clot removal from retinal vasculature, neural probe delivery, and responsive metamaterials. To achieve these goals, shape transformation must occur in SMPs with complex 3D geometries and nanoscale features.

This thesis describes the synthesis and sculpting of a benzyl methacrylate-based SMP into 3D structures with <800nm characteristic critical dimensions *via* two photon lithography. The glass transition based shape memory mechanism of these materials is explored through dynamic nanomechanical analysis of 8μm-diameter cylindrical pillars, which revealed the initiation of a tunable glass transition at 60°C not present in highly crosslinked materials. Shape memory programming of the characterized pillars as well as complex 3D architectures, including flowers with 500nm thick petals and cubic lattices with 2.5μm unit cells and overall dimensions of 4.5μm x 4.5μm x 10μm, demonstrated an 86 +/- 4% characteristic shape recovery ratio. These results reveal a pathway towards SMP devices with nanoscale features and arbitrary 3D geometries changing shape in response to temperature.

This thesis subsequently focuses on a particular potential application for such materials: neural probes designed for deployment in primate brains. Architected shape memory structures have the potential to create favorable long-term recording environments through softening triggered by biological conditions, deployment to beyond tissue damage during initial electrode positioning, and architectural features designed for optimal scaffold-tissue interactions. This thesis addresses one of the barriers to the deployment of such structures: the high loading during centimeter scale insertions required for primate brain targeting is incompatible with buckling free-insertion of low stiffness and/or cross sectional area probes required for minimizing the foreign body response.

Lamb brain tissue model experiments with 280μm diameter platinum coated carbon fiber probes demonstrate that 59+/- 3% of the work during 3cm probe insertion is attributable to friction, suggesting that friction reduction is a favorable approach to load minimization. A phosphorylcholine-based ~100nm low friction coating is used to reduce the shear stress at the probe-brain interface by 20+/-7 %, demonstrating a facile method for friction reduction that has minimal impacts on probe cross sectional area. Surgical validation of probe insertion in a porcine head model reveals that these probes are suitable for whole brain penetration of brains at the primate scale ($\sim 10^2$g). These results show that loading requirements during whole brain penetration can be reduced through addressing the contribution of friction and introduce a viable vehicle for recording electrode delivery to large scale brains.

In summary, this thesis provides the foundation for developing stimuli responsive microscale devices and materials and, in the case of deep brain neural recording, the building blocks for the design of an integrated shape memory/ low friction carbon fiber electrode delivery device. Future research on the scalable fabrication of architected shape memory polymers could enable the widespread application of such materials.

PUBLISHED CONTENT AND CONTRIBUTIONS

[1] L. V. Elliott, E. E. Salzman, J. R. Greer. "Stimuli responsive shape memory microarchitectures" *Advanced Functional Materials,* 2008380 (2020). DOI: 10.1002/adfm.202008380.
L.V.E. performed the experiments, analyzed the data, and wrote the manuscript.

[2] L. V. Elliott, J, Jialiang, R. A. Gallivan, W. Deng, D. Y, Tsao, J. R. Greer. 'Low friction neural probe implantation for long-term recording in large scale brains.' *(Manuscript in preparation).*
L.V.E. fabricated probe samples, performed lamb tissue experiments and Raman spectroscopy, analyzed the data, and wrote the manuscript.

TABLE OF CONTENTS

LIST OF ILLUSTRATIONS

LIST OF TABLES

C h a p t e r   1

INTRODUCTION

Adapted in part from:

1.1 Architected shape memory polymers (SMPs): Applications and mechanisms

Shape memory (SM) materials generating programmable movement in response to temperature changes. A well-known class of SM materials is shape memory alloys (SMAs), with a notable example of nitinol, which is used in devices such as stents, guide wires, and orthodontic braces. SMAs typically deform *via* a phase transformation mechanism, achieving recoverable strains of less than 8%.[1] Shape memory polymers (SMPs) are capable of deforming by >100%, and have therefore garnered widespread attention in areas that do not require the higher stiffness of SMAs, but can benefit from larger scale deformations. These applications include shrink tubing, which has provided electrical and environmental protection to wires since the 1960s and, more recently, self-tightening sutures.[1,2]

Application of macroscale 3D architected SMPs

The range of potential applications for SMPs has expanded with the introduction of precise control over architecture through 3D printing methods. One key area is biomedical device design, which can benefit from the deployable structures with complex 3D geometries. Acrylate-based multi-material printing *via* projection microstrealithography enables the fabrication of cardiovascular stents with minimal geometric constraints, achieving the structural complexity necessary for actuation (**Figure 1.1a**). [3,4] The flexibility of the 3D printing techniques allows the integration of optimal geometries, such as auxetic structures

that provide improved strength at minimal artery surface coverage and the high contraction-expansion ratios necessary for efficient deployment.[5] SMPs can also be used to produce personalized deployable devices, such as tracheal stents that undergo minimal migration due to precise anatomical matching based on imaging data (**Figure 1.1b**).[6]

Further, architected SMPs have found applications in soft robotics, which aims to incorporate large deformations, complex motions, and arbitrary geometries into robot design to achieve safe interaction with people and fragile objects. Projection micro stereolithography fabrication of SMPs can produce temperature responsive grippers for such robots, enabling autonomous response to external stimulus (**Figure 1.1c**).[3] SMPs can also be integrated into flexible electronics systems, for example as a temperature sensor where a heat triggered structural change closes a circuit (**Figure 1.1d**).[7]
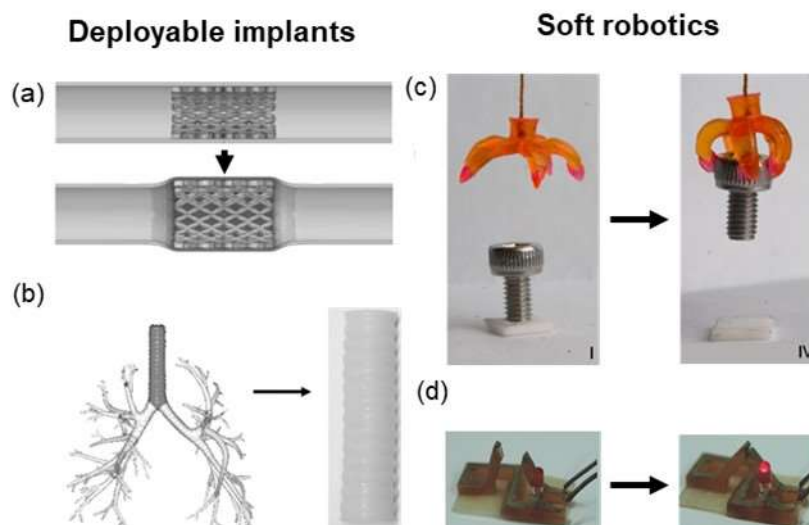
Figure 1.1. Applications of macroscale architected shape memory polymers. (a) Schematic illustrating architected stent deployment in an artery.[4] *Reproduced with permission.* (b) Schematic of tracheal stent placement and an image of the personalized printed device.[6] *Reproduced with permission.* (c) Temperature responsive gripers fabricated via stereolithography.[3] *Reproduced under the creative commons license.* (d) A circuit actuating in response to a temperature change.[7] *Reproduced with permission.*

Mechanisms governing synthesis of shape memory polymers

Actuating a shape memory response requires implementing a programming protocol on a polymer network optimized for entropic energy storage. The mechanism of thermally-driven shape memory involves three steps: (1) deforming a polymer structure at elevated temperatures, where applied loads drive entropically unfavorable changes within polymer chain conformations, followed by (2) decreasing the temperature to lock the programmed shape by trapping molecular microstructure in its low entropy configuration through a molecular mobility-suppressing thermal transition, and (3) heating the structure to overcome the enthalpic barrier to recover its original shape.[1,8] Fabricating SMPs with 3D geometric control requires implementing this shape change mechanisms in polymer networks amenable to 3D printing, two classes of which are discussed below.

Crystallization driven SMPs: Shape memory networks are generally composed of flexible chain segments and netpoints. Netpoints are crosslinking sites that define the permanent shape of the material and provide stability, and can be based on covalent bonds, crystals with high T_m, or other intermolecular interactions, as long as they remain intact when temperature is increased and the structure is deformed during programming. Upon cooling under the programming load, additional temporary netpoints form *via* crystallization and prevent the recoiling of chain segments oriented during deformation. Recoiling, and therefore original shape recovery, occurs when the temperature is elevated such that the temporary netpoints melt.[1]

Glass transition driven SMPs: Glass transition driven SMPs are also composed of flexible chain segments and netpoints, with temporary netpoint formation driven by vitrification rather than crystallization. Since micro-Brownian motion is frozen below the glass transition temperature, polymer chain segments are prevented from recoiling when cooled during programming (**Figure 1.2**).[8] Glass transition-based programming offers a number of advantages over a crystallization-based approach, including greater tunability of the transition temperature.[8] It can also enable fabricating structures with near room temperature

transitions through light activated methods, without encountering crystal-induced scattering or requiring resin heating to avoid crystallization.[7] We will therefore focus on this mechanism for the remainder of the thesis.
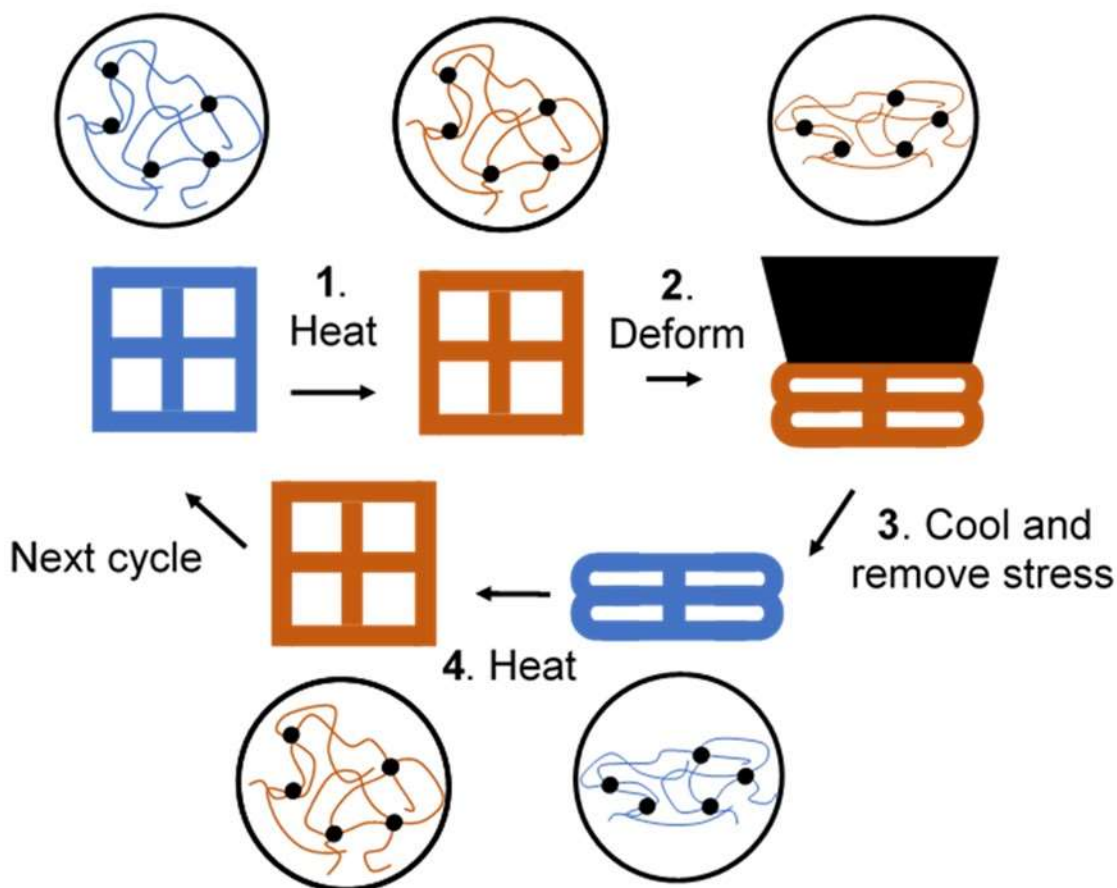
Figure 1.2. Glass transition based shape memory programming. Covalent crosslinks are represented by black circles. Polymer chains are represented by blue or orange lines, with the colors reflecting room temperatures and elevated temperature, respectively. **Step 1**: A loosely crosslinked network is heated from glassy state (blue) to above its glass transition temperature (rubbery state, orange). **Step 2**: The structure is mechanically deformed into the desired configuration. **Step 3**: The programming stress is maintained while the structure is cooled to its glassy state (blue); at that time, the load is removed, and the structure remains in the programmed configuration. **Step 4**: Heating the structure to above glass transition induces shape recovery (orange) as the polymer chains regain mobility and return to their original, more entropically favored configuration. *Adapted from [1]*.

1.2 Microscale 3D architected SMPs

Potential applications of microscale 3D architected SMPs

Attaining full 3D design freedom in microscale structures can further expand the applications of SMPs. Miniaturization of SMP structures that currently exist on the macroscale will enable targeting of environments with restricted real estate, facilitating the transition of existing therapies to new targets.

One example is the potential to expand clot removal techniques developed for ischemic stroke to smaller targets such as retinal vasculature. Currently available treatments for ischemic stroke include mechanical thrombectomy devices. These tools, in conjunction with pharmacological treatments, can remove clots blocking blood flow within the brain and improve the probability of a patient living independently post stroke from 20% to 33%. [9] The nitinol-based shape memory devices can coil around a clot in a shape similar to a cork screw to enable retrieval through a microcatheter.[10] Alternative geometries include mesh networks that expand as stents, push the clot against the artery wall, and become embedded within it, also enabling retrieval.[11]

While ischemic stroke clot retrieval devices target vasculature down to the 2mm diameter, clots can also block ocular vasculature with typical diameters of 80-100μm.[12, 13] Such clots cause retinal vein occlusion, which affects 16.4 million adults worldwide and, after diabetic retinopathy, is the second leading cause of blindness.[14] Recent advancements in robotic surgery can reduce physiological tremor (~ 100μm) and enable precise force sensing to facilitate surgical procedures that access the occluded veins.[15] Implementing mechanical thrombectomy analogous to ischemic stroke treatments in these procedures could enable removal of mature fibrin crosslinked thrombi that are resistant to drug therapy and avoid systemic pharmacological side effects (ex. bleeding into the brain).[9] This necessitates the development of shape memory devices with footprints of <100μm with complex architectures similar to macroscale ischemic stroke analogues.

Complex microscale SMP structures could also enable a suite of new applications specific to their scale. These applications can utilize uniquely functional architectures available at the microscale or manipulate cell/scaffold interactions:

1) *Microscale metamaterials:* Shape memory effects could be introduced to mechanical metamaterials that are currently only accessible via TPL. The high resolution of TPL enables the fabrication of materials with precisely defined structures that result in unique mechanical properties, such as high strength-to-weight ratios, damage resistance, compression induced twisting, and mechanical cloaking.[16,17,18,19] These properties arise from structural design, rather than the characteristics of the particular constituent solid. With shape memory polymers as the constituent solid, these architectures, and therefore their mechanical properties can be altered in response to stimuli.

2) *Neural probe delivery:* Long term single-neuron recording can enable brain connectome mapping and precise drug response studies for better insight into disorders such as Alzheimer's and depression.[20] To achieve these goals, the foreign body response due mechanical damage induced by recording electrodes must be minimized.[21] The slow deployment enabled by shape memory polymers can minimize acute damage, and control over structure architecture can enable optimal cell/material interaction.[22,23] This combination of optimal structure and deployment, combined with damage minimizing minimal footprint (< 200µm), can be achieved through the development of architected microscale shape memory electrodes.

Microscale shape memory response *via* glass transition

Transferring the glass transition-based shape memory mechanism from the macro to the microscale faces obstacles due to the reduced size of the network and imperfections that may become significant at the target scale.

Reduced number of elastically active chains: The shape memory capacity of individual features is limited by the reduced number of polymer chains and crosslinks compared to macroscale materials. Based on Kuhn's classic affine network model, the number of elastically active chains per unit volume is given by **Equation 1.1** below

$$\frac{n}{V} = \frac{G}{k_B T}$$ (1.1)

where n is the number of elastically active chains in a material volume V, G is the shear modulus of the polymer , k_B is the Boltzmann constant, and T is the temperature in Kelvin.[24] Assuming that the elastic properties and polymer chain cross-linking density are uniform throughout the sample, the number of elastically active polymer chains within a volume of typical acrylate-based shape memory polymer with a rubber plateau modulus of ~10MPa should decrease from ~10^{15} in a volume of 1 mm^3 to ~10^6 chains in a 1μm^3 volume. Since entropic energy is proportional to the number of chains, this decreases the energy stored in each architectural feature.[25]

Nanoscale inhomogeneities: The energy storage potential of microscale shape memory structures may be decreased by nanoscale heterogeneities in crosslinked networks. The distribution of network defects produced through free radical polymerization results in clusters of high and low crosslinking density, as reported by di Lorenzo et al.[26] These high crosslinking density clusters contain short molecular strands, with lengths close to the persistence length of the polymer, rendering them too rigid to deform and store elastic energy, and effectively reducing the number of functional elastic chains in an individual feature. A typical cluster size is on the order of tens of nanometers, resulting in some cases in a two-fold increase in the effective crosslink density on a ~100nm scale as compared to the macroscopic average for the same material.[27] This localized decrease in entropically active chains could compromise the ability of isolated nanoscale features of SMP structures to store entropic energy, and therefore demonstrate the shape memory effect though a glass transition.

1.3 Outline and objectives

The aim of this thesis is to synthesize architected microscale shape memory structures, explore their shape memory mechanism and response at the relevant scale, and finally address a barrier to their potential applications in neural probe design. Specifically, the second chapter discusses an approach to fabricating shape memory materials directly *via* two-photon lithography. The third chapter explores the glass transition that enables their shape memory response through *in-situ* nanomechanical characterization. The fourth chapter demonstrates shape memory behavior in a variety of structures, illustrating the versatility of this approach as well as the challenges of microscale shape memory programming. The fifth chapter focuses on one potential application for these materials: the delivery of electrodes to large-scale brains for long term neural recording. Specifically, we address the challenge of delivering shape memory architectures to recording sites centimeters deep within the brain through friction minimization. In the end, we discuss open questions and future research directions, including designing a full shape memory enabled deep-brain neural recording device and a pathway to scalable production of nano architected shape memory materials.

Chapter 2

DESIGN, SYNTHESIS, AND MICRO-FABRICATION OF SHAPE
MEMORY POLYMERS (SMPS)

Adapted in part from:

2.1 Introduction

State of the art in microscale shape memory structures

Shape memory effects in polymers at the micro and nano scale have been mainly explored in patterned films, for example in 2mm thick polyurethane and 6mm thick thermoset-epoxy based films patterned with PDMS and silicon molds to produce 10µm and 20µm surface features, respectively.[28,29] Temperature-induced changes in the morphology and dimensions of the various surface features on such films, such as grooves (300nm-50µm), pillars (500nm – 50µm), and pyramids (20-150µm), have resulted in controllable adhesive,[28,29] optical,[30] and wettability properties,[31] and have been utilized in devices with reconfigurable microfluidics channels[32] and substrates with variable cell attachment.[33, 34] 3D patterning of shape memory films has also been demonstrated, for example by Niu et al. who fabricated polyurethane based structures with ~300nm pores through nanoparticle templating for photonic crystal applications.[35] This fabrication method is restricted to periodic patterns, and similarly to the surface patterned films, produces polymer networks with dimensions on the millimeter scale. In all of these cases, while the films display the shape memory effect through crystallization and glass transition mechanisms, it is not possible to isolate the entropic energy stored in individual micro or nanoscale features, as they are interconnected or attached to an underlining SM substrate.

Shape memory effects in isolated microscale SMPs have been limited to molded structures, which are dominated by 2D designs and their projections (2.5D). PDMS molding fabrication methods have been used to create shapes such as spheres, cubes, and boomerangs from crystallization-based shape memory materials.[36-38] Miniaturization of SMPs with more complex structures has been a challenge: micro-stereolithography fabrication is limited by its resolution of ~10μm, and existing higher resolution approaches, i.e. two-photon lithography (~5μm), require molding.[39,40]

Two-photon lithography direct laser writing for SMP polymerization

To achieve geometric complexity in microscale SMP structures we focused on the development of an SMP resin directly compatible with two photon lithography direct laser wring (TPL-DLW). In this fabrication technique, free radical polymerization occurs within the focal region of a femtosecond laser (**Figure 2.1**). This is enabled by a photoinitiator that is excited by absorbing two photons simultaneously. As the absorption rate of energy is proportional to the square of light intensity, the cross section of two photon absorption is much lower than in a one-photon absorption process. Further, polymerization only begins above a certain threshold of radical concentration due to oxygen radical quenching. Together, optical nonlinearity and thresholding restrict polymerization to the focal point of the beam and enable resolution beyond the diffraction limit.[41] Therefore, rastering the focal point in 3D space creates structures with nearly arbitrary geometry and features on the submicron scale. The technique has produced a variety of microscale devices and architected structures with unique mechanical properties.[17-19]
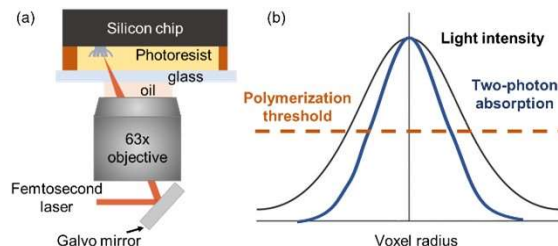
Figure 2.1. Schematic illustration of two photon lithography direct laser writing. (a) Two-photon lithography experimental set up where the motion of a femtosecond laser is controlled by a galvo mirror to define a 3D geometry. Not drawn to scale. *Adopted from [1]*. (a) Schematic illustrating the Gaussian laser beam intensity (black) and the square of that intensity, to which two photon absorption is proportional (blue). Intersections with the polymerization threshold illustrate one of the mechanisms for reduced voxel size in two-photon lithography.

Two-photon lithography utilizes a narrow range of exposure doses to polymerize resins with low degrees of conversion, and therefore typically utilizes highly functional monomers (ex. pentaerithritol triacrylate) to enable sufficient crosslinking to maintain structural integrity.[42-44] To develop structures with shape memory properties that undergo a glass transition, the polymer network has to instead be dominated by monofunctional polymerized chains (typically 60-90wt%).[3] We developed such an acrylate-based shape memory resist by combining 7-diethyalmamino-3-thenoylcoumarin (photoinitiator) with an amine functionalized methacrylate (chain builder 1), and an amine functionalized diacrylate (crosslinker) and benzyl methacrylate (chain builder 2), whose chemical structures are shown in **Figure 2.2**. In this chapter, we describe how this composition and the corresponding micro-fabrication approach (1) enable TPL-DLW fabrication of loosely crosslinked networks necessary for glass transition driven shape memory and (2) introduces versatile chemical functionality to microscale SMP structures.
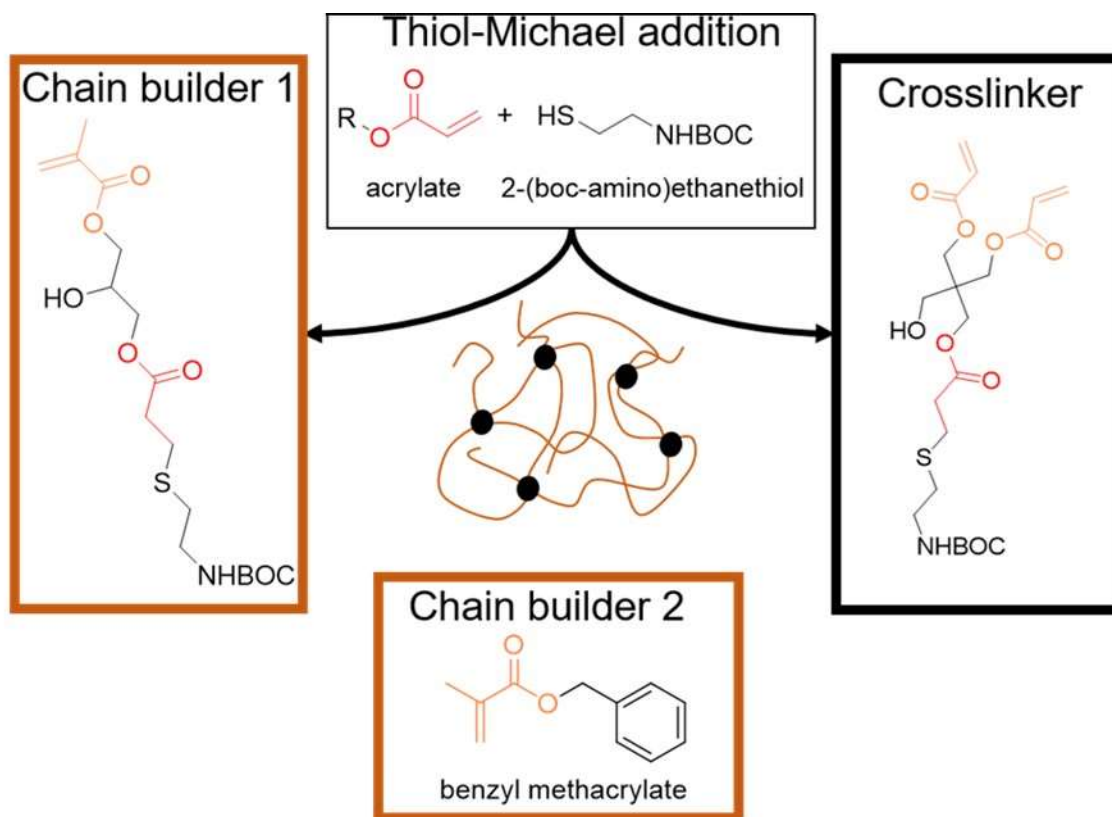
Figure 2.2. Chemical composition of the developed shape memory resin. Chemical structure of a functional chain builder (chain builder 1) and crosslinker synthesized via the thiol-Michael reaction and benzyl methacrylate (chain builder 2). Functional groups highlighted in orange are available for free radical polymerization during TPL to form the loosely crosslinked network. *Adopted from [1].*

2.2 Tailoring the micro-fabrication approach to shape memory polymer network design

Benzyl methacrylate for shape memory programming

Benzyl methacrylate (BMA) is a monomer commonly used in macroscale shape memory network synthesis. Crosslinked acrylate systems containing BMA exhibit relatively high strains to failure, failure strengths, and toughness. This is attributed to high cohesive energy density derived from benzene ring stacking, which increases resistance to fracture during large scale deformations.[45] These properties are advantageous for shape memory materials to facilitate high strains during the programming phase of the SMP cycle.

Pre-Polymerization for two-lithography compatibility
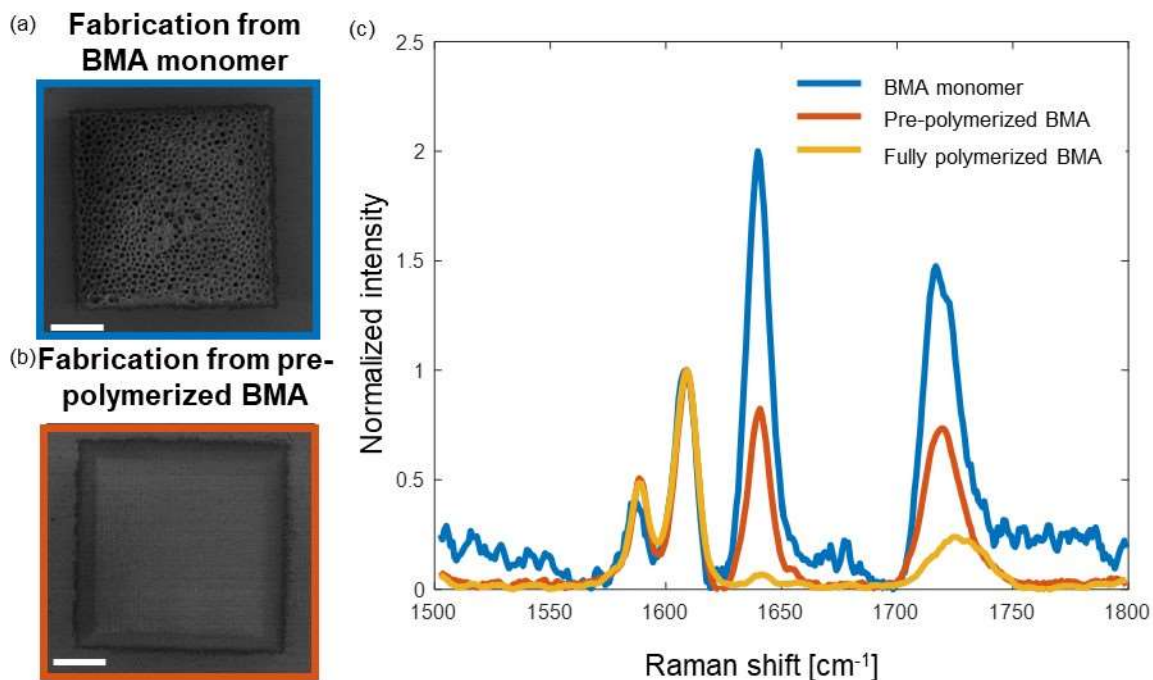
Figure 2.3. Benzyl methacrylate pre-polymerization. a) A plate fabricated via TPL-DLW directly from a resist that directly incorporated benzyl methacrylate (BMA) monomer. Scale bar 10µm. b) A plate fabricated via TPL-DLW from a resist that incorporates pre-polymerized BMA. Scale bat 10µm. c) Representative Raman spectra used to determine benzyl methacrylate degrees of polymerization. Intensities are normalized by the aromatic C=C stretch peak at 1605 cm^{-1}. *Adopted from [1].*

Prior to incorporation into the resist, BMA monomers were partially polymerized under flood UV light (36W) for 5 minutes to avoid excessive micro bubbling during TPL-DLW that occurred when the monomers were added to the resin directly **(Figure 2.3a-b)**. Micro bubbling occurs in TPL-DLW at increased energy dosages and commonly sets the upper threshold of laser power during fabrication.[46] In SMP resins formulated without pre-polymerization, bubbling occurred at the polymerization threshold, eliminating the polymerization window. Previous studies have suggested that micro bubbling occurs when a local increase in temperature during exothermic polymerization results in monomer evaporation.[42] Increase bubbling is therefore consistent with the boiling point on benzyl

methacrylate (98°C) being lower than the boiling point (427°C) and flash point (152°C) of the typically utilized pentaerithrotol triacrylate. The up to several hundred degrees temperature rises expected from exothermic polymerization and vibrational relaxation of photo initiator molecules are therefore likely triggers for micro-bubbling at the initiation of polymerization for a benzyl methacrylate-based resist.[47] The increase in energy dosage required to initiate bubbling in pre-polymerized resins can then be attributed to the increased boiling point of oligomers and/or the reduced number of unreacted acrylate groups available for further exothermic polymerization.

Raman spectroscopy was performed on pre-polymerized BMA to ensure that acrylate groups were available for further reaction during two-photon polymerization. To estimate the degree of polymerization, the peak areas corresponding to aromatic (1605 cm^{-1}) and aliphatic (1635 cm^{-1}) carbon double bonds were determined by trapezoidal numerical integration.[48] The ratio of these areas for the polymerized material and the starting monomer were then compared since, unlike the carbonyl C=O stretch (1730 cm^{-1}), the aromatic C=C stretch peak is not expected to be affected by polymerization. The degree of polymerization was defined as:

$$DP\% = \left(1 - \frac{R_{polymer}}{R_{monomer}}\right) * 100\%$$

$$R = \frac{A_{aliphatic}}{A_{aromatic}}. \tag{2.1}$$

The calculation was performed based on 3 samples of pre-polymerized BMA. A set of representative Raman spectra, normalized by the aromatic peak at 1605 cm^{-1}, is provided in **Figure 2.3c**. The degree of polymerization was determined to be 60 $^{+}/_{-}$ 3%. For comparison, the degree of polymerization for BMA exposed to UV light for 1 hour (fully polymerized) was determined to be 97 $^{+}/_{-}$ 1% This suggests that the benzyl-methacrylate incorporated into the TPL-DLW resist is a mixture of monomers and oligomers. Further characterization of the pre-polymerization product by Gel Permeation Chromatography (GPC) indicates a molecular weight of Mn= 3.1 +/- 0.2 x10^4 g mol^{-1} and a polydispersity index (PDI) of 1.80 +/- 0.07, supporting this interpretation. **Figure 2.4** shows the Raman spectra of samples microfabricated with the pre-polymerized BMA-based resist and flood

UV-exposed (non-patterned) samples as control; both contain peaks at 1004 cm⁻¹, 1030 cm⁻¹, 1130-125 cm⁻¹, and 1585-1605 cm⁻¹, which are associated with benzene rings, and a peak at 1730 cm⁻¹, which is associated with carbonyl groups. The close match between peaks observed in the two samples confirms that benzyl methacrylate is incorporated into the final microscale structures after development.

Wave number [cm⁻¹]	Feature
940-960	Silicon chip
1004, 1030	Benzene ring breathing, deformation (in plane)
1130-1215	Benzene ring deformation (in plane)
1370-1380	CH₃ symmetric bending
1450	CH₂ scissoring
1585-1605	Aromatic C=C stretching
1635	Aliphatic C=C stretching
1730	C=O stretching
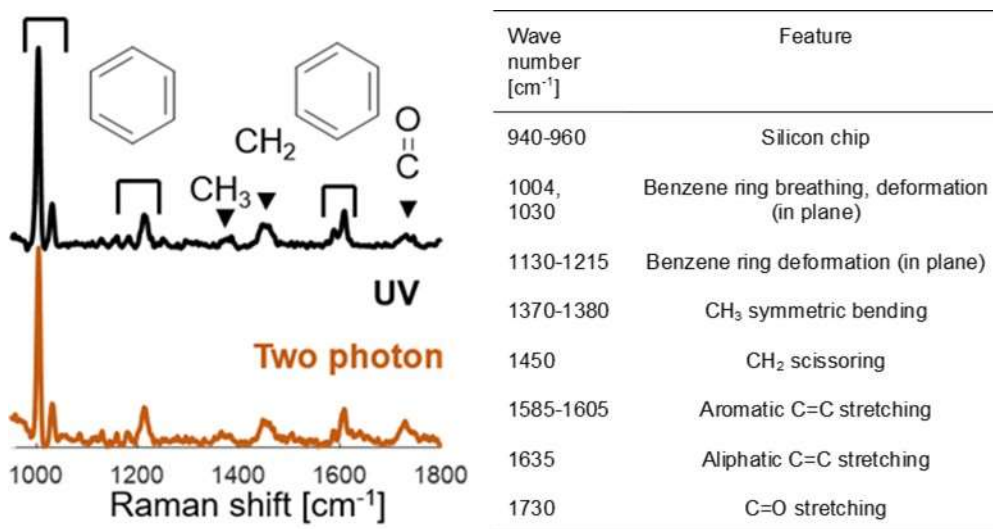
Figure 2.4. Raman spectroscopy of micro-fabricated and flood polymerized BMA resin-based samples. Raman spectra of a bulk sample polymerized with flood UV exposure (black) and pillars polymerized via TPL-DLW (orange) and corresponding peak assignments.[48, 49] *Adopted from [1]. Peak assignment courtesy of Erika Salzman.*

Microfabrication

Writing parameters: Two-photon lithography writing parameters were tuned to enable fabrication with the pre-polymerized resist. The low degree of conversion characteristic of TPL-DLW, combined with the reduced number of acrylate groups available for polymerization during writing with the developed resist, required tuning parameters to maximize crosslinking. Crosslinking density is inversely proportional to intervoxel spacing, as demonstrated by TPL-DLW fabricated hydrogels that display writing parameter controlled degrees of swelling.[50,51] In samples where intervoxel spacing in the x-y plane (hatching distance) was increased from 50nm to 100nm, 67% volume shrinkage

was observed post development, suggesting that at lower degrees of crosslinking, unreacted monomers and uncrosslinked benzyl methacrylate oligomers diffused from the structure (**Figure 2.5**).
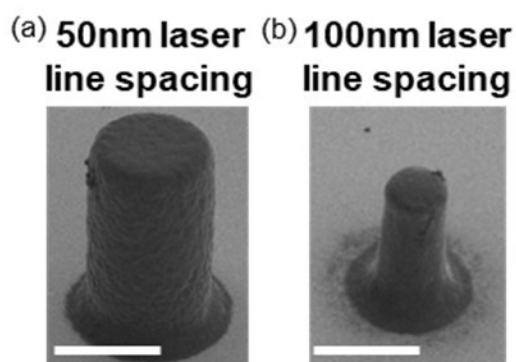
Figure 2.5 Microstructure shrinkage controlled by fabrication parameters. SEM images of pillars fabricated with (a) 50nm laser line spacing in the x-y plane and (b) 100nm laser line spacing under otherwise constant fabrication and development parameters. Scale bars 10μm.

Structure versatility: To demonstrate the versatility of architectures attainable by this methodology, we fabricated a variety of different form factors, including lattices with beam diameters of 780nm (**Figure 2.6a**), a prototype stent with 4μm beams (**Figure 2.6b**), and a flower with 500nm thick petals (**Figure 2.6c**).
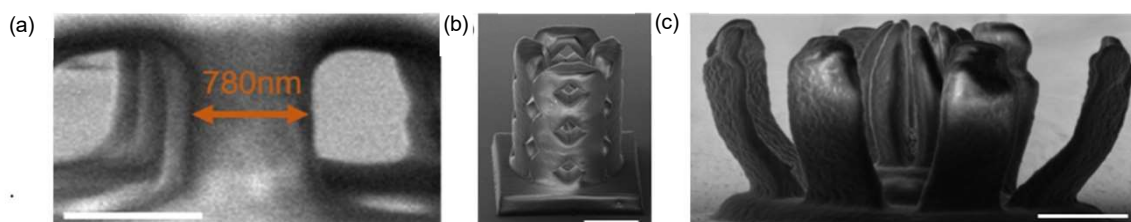
Figure 2.6. Microfabrication of versatile SMP 3D architectures. SEM images of representative TPL-produced SMP architectures: (a) an individual 780nm-diameter beam of a cubic nanolattice (Scale bar 1μm), (b) a prototype stent structure with 4μm beams imaged at a 30° tilt (Scale bar 10μm), and (c) a flower with minimal petal width of 2μm and thickness of 500nm (Scale bar 5 μm). *Adopted from [1].*

Substrate versatility: Structures we generally fabricate on acrylate functionalized silicon chips in a sandwich configuration to provide a stiff substrate for mechanical test. Through manual interface finding, it was also possible to use the same configuration to fabricate samples on AFM cantilevers and polyvinyl pyrrolidone (PVP) layers spin coated on silicon. PVP layers can then be dissolved in minimal water to obtain free-standing structures.

2.3 Incorporating chemical functionality

The amine functionalized components were synthesized through 1:1 base catalyzed thiol-Michael addition, which is an addition of an enolate type nucleophile to an α,β-unsaturated carbonyl. The enolate in this case is 2-(BOC-amino)-ethanethiol, which features a BOC protected amine group. As the first carbonyl, we chose 3-(acryloxy)-2-hydroxypropyl methacrylate, which can act as a chain builder in the shape memory network after the thiol-Michael addition because it contains both an acrylate and a methacrylate group. The latter is resistant to thiol-Michael addition due to the electron donating effect of the methyl group, allowing the acrylate group to react preferentially.[52] We confirmed this selectivity using ^{1}H NMR, which contained hydrogen signals from the methacrylate only, and not from the acrylate (**Figure 2.7**). The unreacted methacrylate groups are expected to undergo free-radical polymerization during TPL-DLW and to contribute the flexible chain structure components to the resin. For the thiol-Michael synthesis of the crosslinker, we chose pentaerithritol triacrylate as a carbonyl because, in a 1:1 molar ration with a thiol, it is expected to produce a statistically determined distribution of products.[53] The average product is expected to contain two acrylate groups (**Figure 2.8**), which are available for free radical polymerization and can contribute to a loosely crosslinked network. ATR (Attenuated Total Reflectance) FTIR spectroscopy of the micro-fabricated structures produced by incorporating these synthesized components into the resist confirms the presence of BOC-protected amine groups, as indicated by a broad peak at 3300cm^{-1} associated with the amine N-H stretch (**Figure 2.9**).[54]
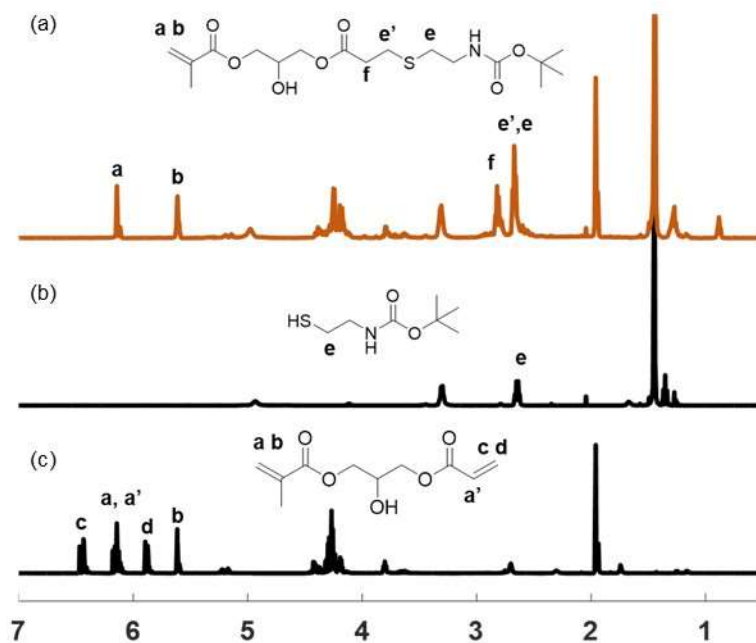
Figure 2.7. NMR of chain builder functionalization. a) ¹H NMR of the thiol-Michael addition product used as the functional chain builder. Peaks corresponding to methacrylate hydrogens are highlighted, as well as those corresponding to the reacted acrylate groups. b) ¹H NMR spectrum of the 2-(BOC-amino) ethanithiol starting material. c) ¹H NMR spectrum of the 3-(acryloyloxy)-2-hydroxypropylmethacrylate starting material. Peaks corresponding to the acrylate and methacrylate groups are noted. *Adopted from [1].*
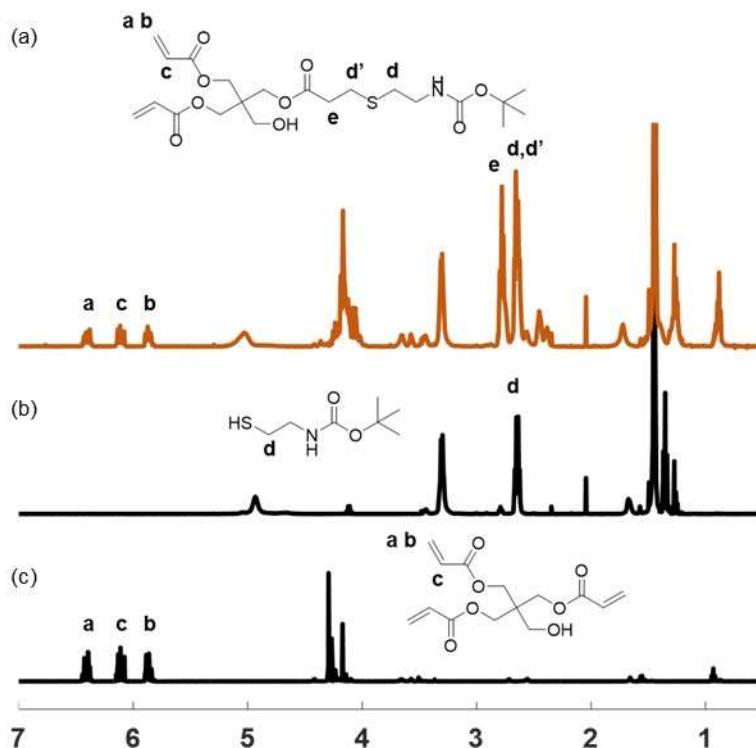
Figure 2.8. NMR of crosslinker functionalization. a) ^{1}H NMR spectrum of the thiol-Michael product used as the crosslinker. Peaks corresponding to reacted and unreacted acrylate groups are highlighted. b) ^{1}H NMR spectrum of the BOC-ethanethiol starting material. c) ^{1}H NMR spectrum of the pentaerythritol triacrylate starting material. Peaks corresponding to the acrylate groups are highlighted. *Adopted from [1].*
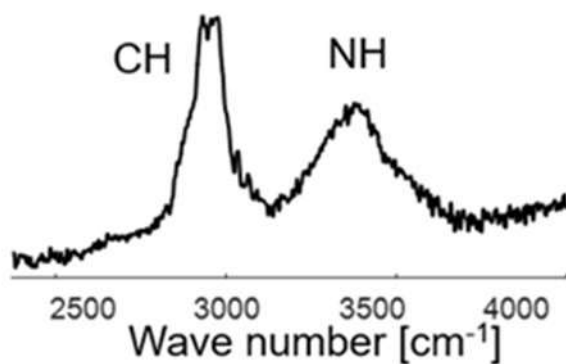
Figure 2.9 ATR-FTIR spectrum of microfabricated pillars. The peak at 3300 cm^{-1} coveys the presence of amines.[54] *Adopted from [1].*

2.4 Summary and outlook

We developed a two-photon lithography resin targeted at shape memory applications. As confirmed by Raman spectroscopy, structures fabricated from this resin incorporate monofunctional acrylates, as desired for glass transition based shape memory actuation. As demonstrated by ATR-FTIR, the resin also incorporates amine groups. Structures fabricated from this material demonstrate versatility in 3D architectures with sub-micron features previously inaccessible for microscale shape memory polymers. As the glass transition based shape memory mechanism depends primarily on the structure of the molecular network rather than on a specific chemical repeat unit, the chemical and mechanical properties of a shape memory network can be tuned and optimized for a particular application by properly choosing the network building components and polymerization conditions without significant limitations.

In the particular case of this work, the composition of the synthesized shape memory resist was designed to be amenable to surface chemical functionalization. The amine functional groups that populate the surfaces of 3D micro-architected SMPs in this work can add functionality by, for example, conjugating to proteins for improved adhesion to biological substrates or to light or magnetic field-responsive nanoparticles that can enable remote activation of the shape memory effect.[55,56] Further, the facile click chemistry used to access this particular functionality can also be used to install a variety of functional groups that can alter properties such as wettability without requiring purification or adversely affecting two-photon polymerization.[53,57]

The shape memory resist compositions can also be tuned to achieve desired mechanical properties. In this case, the monomer benzyl methacrylate was incorporated to enable large deformations, and the chain building component has high cohesive energy density, which results in a substantial strain-to-failure.[45] The developed microscale shape memory system is therefore highly tunable and can be adjusted to a variety of applications.

2.5 Experimental methods

Materials

Pentaerythritol triacrylate (PETA) (technical grade, Sigma Aldrich), 3-(acryloyloxy)-2-hydroxypropylmethacrylate (Sigma Aldrich), benzyl methacrylate (BMA) (96%, Sigma Aldrich), 2-(BOC-amino) ethanethiol (97%,Sigma Aldrich), hexylamine (99%, Sigma Aldrich), Ethyl phenyl (2,4,5-trimethylbenzoyl) phosphonate (TPO-L) (RahnUSA Corp.), acetic acid (≥99%, Sigma-Aldrich), ethyl alcohol (95%, Koptec), 3-(Trimethoxysilyl)propyl ethacrylate (98%, Sigma Aldrich), 7-Diethylamino-3-thenoylcoumarin (DETC) (Exciton), propylene glycol monomethyl ether acetate (PGMEA) (>99.5%, Sigma Aldrich), isopropyl alcohol (IPA) (99.7%, Sigma Aldrich), dichloromethane (DCM) (>99%, Alfa Aesar), phosphoric acid (85%, Alfa Aesar), sodium bicarbonate (>99.7%, Sigma Aldrich), Orange II sodium salt (>85%, Sigma Aldrich), and hydrochloric acid (36.5-38%, J. T. Baker) were used without further purification.

Photoresist Preparation

Benzyl Methacrylate Polymerization: Benzyl methacrylate (5.9 mmol, 1ml) was combined with TPO-L (0.05 mmol, 14μL), and polymerized under a UV lamp (36W, DR-301C, MelodySusie) for 5 minutes while stirring vigorously. The samples were then submerged in an ice bath to quench the reaction and stored wrapped in aluminum foil.

Thiol-Michael Addition Reactions: To functionalize the methacrylate chain builder, 3-(acryloyloxy)-2-hydroxypropyl methacrylate (1.0 equiv., 1.1 ml, 5.9 mmol) and 2-(BOC-amino) ethanethiol (1.0 equiv., 1ml, 5.9 mmol) were combined in a 10ml vial while stirring in an ice bath. Hexylamine catalyst (0.1 equiv., 156 µl, 0.59 mmol) was then added dropwise and the solution was stirred for 30min as it became increasingly viscous. The completion of the reaction was verified ^{1}H NMR, and the product was used without further purification. To functionalize the crosslinker, a procedure similar to that reported by Yee et al. for pentaerythritol tetraacrylate functionalization was followed.[53] Pentaerythritol

triacrylate (1.0 equiv., 189 µL, 0.75mmol) and 2-(BOC-amino) ethanethiol (1.0 equiv., 127 µL, 0.75 mmol) were combined in a 4ml vial while stirring in an ice bath. Hexylamine catalyst (0.1 equiv., 20µ, 0.075mmol) was added dropwise, and the solution was stirred until impeded by the viscosity of the liquid (~10min). To minimize transfer of the viscous liquid, all components of the resin were combined in this vial.

Photoresist formulation: To formulate the resist, pBMA (1.4g, 67.6 wt%) and functional chain builder (0.3g, 14.5wt%) were added to the functional crosslinker (0.37g, 17.9wt%), and stirred overnight to homogenize without exposure to ambient light. A solution of the photo initiator DETC (4.5 mg) in DCM (20µL) was then prepared and combined with 200µL of the mixture. The resist was stirred, wrapped in aluminum foil, and refrigerated for storage.

Microfabrication

Functionalized silicon chip preparation: To ensure that the printed structures were securely attached to the silicon chip, the chips were functionalized with acrylate groups prior to polymerization. The chips were ultrasonicated in IPA for 20 minutes and dried with nitrogen. A solution of 95% ethanol and 5% water was adjusted to an approximate pH of 5 with acetic acid. 3-(Trimethoxysilyl)propyl methacrylate was added with stirring to obtain a 2% final concentration. The silicon chips were then dipped in the solution for 5 minutes, dipped in ethanol, and cured at 110 °C for 15 minutes.

Two-photon lithography: Two-photon lithography was performed on the commercial Photonic Professional GT, Nanoscribe GmbH system. The Zeiss Plan-Apochromat 63x/1.4 Oil DIC objective was utilized. The laser power was set at 30 mW with a scan speed of 2,000 µm s^{-1}. To prepare the sample, photoresist (~5 µL) was drop cast onto a glass substrate 30mm in diameter and 0.17mm thick. A functionalized silicon chip was then placed over the droplet, with a ~100µm Kapton tape spacer. The structures were written on the chip via TPL with 50nm hatching distances and 100nm slices. The structures were developed in PGMEA for 1

hour, followed by immersion in IPA for 1 hour. Structures were then critical point dried (Autosamdri 931.GL, Tousimis Research Corporation).

Gel Permeation Chromatography (GPC)

GPC was carried out in THF on two PLgel 10µm mixed-B LS columns (Polymer Laboratories) connected in series with a DAWN EOS multiangle laser light scattering (MALLS) detector and an Optilab DSP differential refractometer (Wyatt Technology). The literature d*n*/d*c* value of 0.144 for poly benzyl methacrylate in THF was used.[58]

Spectroscopic characterization

^{1}H NMR Spectroscopy: NMR spectra were obtained in deuterated chloroform on a Varian 500MHz spectrometer. Chemical shifts were referenced to $CDCl_3$ (δ=7.26 for ^{1}H).

Raman Spectroscopy: Raman data were collected for both macroscale samples (photoresist polymerized under UV light) and TPL microstructures using a Renishaw M1000 Raman Spectrometer system under 783.7 nm incident laser radiation. Five accumulations at 10 seconds each were obtained. Spectra were baseline corrected and smoothed.

ATR-FTIR Spectroscopy: ATR-FTIR data was collected for TPL-DLW synthesized pillars using the Nicolet iS50-FTIR (Thermoscientific) and the Dura Scope (SensIR Technologies). A DTGS KBr detector and a KBr beam splitter were used to perform 30 scans.

Scanning Electron Microscopy

SEM imaging was performed using the FEI Versa 3D DualBeam (FEI co.) and the FEI Quanta 200 at 1-2kV current. No conductive coating was applied.

C h a p t e r   3

DYNAMIC NANOMECHANICAL CHARACTERIZATION TO PROBE GLASS TRANSITION IN SMPS

Adapted from:

3.1 Introduction

Dynamic nanomechanical analysis of shape memory materials

Dynamic mechanical analysis (DMA) is a sensitive technique for identifying polymer glass transitions by tracking the loss and storage moduli, as well as their ratio, tangent delta. In this technique, oscillatory stress is applied to a preloaded structure at a particular frequency, resulting in oscillatory strain. In the glassy state, the polymer is expected to behave as a linear solid, with strain proportional to stress, resulting in stress and strain signals that are in phase (phase shift $\delta = 0^0$). In the rubbery region, the polymer's behavior resembles that of a viscous liquid, with strain proportional to the rate of change in stress. In the limiting case, the stress and strain are out of phase ($\delta = 90^0$). Therefore, the transition from a glassy to a rubbery state can be observed by tracking the $\tan(\delta)$ as a function of temperature. Throughout this transition, the energy stored during deformation is characterized by the storage modulus, while energy dissipated as heat is characterized by the loss modulus. These values can be calculated based on the phase shift as well as the stress and strain amplitudes.

DMA is a powerful approach to guiding SMP programming through glass transition characterization. As detected by DMA, a polymer's stiffness decreases sharply when entering the glass transition region, which is attributed to an increase in kinetic energy and free volume. Deformation in this regime occurs *via* chain slippage and, optimally for shape

memory materials, conformational changes and chain elongation.[59] This increases chain ordering, thereby decreasing conformational entropy. The increased entropy results in a retractive force, which counteracts further elongation and is given by equation 4 below.

$$\sigma_R = \frac{\rho RT}{M_i}[\alpha - \frac{1}{\alpha^2}] \tag{3.1}$$

Here ρ is the density, R is the gas constant, T is the temperature, M_i is the molecular weight between crosslinks, and α is the extension ration. The entropic retractive force becomes increasingly important at elevated temperatures, which means that optimal energy storage occurs at the initiation of the glass transition.[59] Experimentally, this is confirmed by maximum storable strain for crosslinked amorphous SMPs being observed within the region.[60]

Glass transition characterization on the microscale

Characterization of microscale samples rather than bulk material is necessary to account for polymerization technique dependent variability in the degree of crosslinking and for the influence of microscale sample size, if any, such as surface area or defect density related effects. Standard DMA instruments are generally not compatible with microscale sample sizes because they are designed for millimeter-sized samples, and the minimum force resolution of 10μN prevents sufficiently accurate deformations.

Nanoindentation instruments can resolve forces on the order of 3nN and have been employed by the nanomechanics community to characterize time-dependent properties of polymer samples. For example, Hayes *et al.* used dynamic nanoindentation to characterize the mechanical properties of different polymer films, including an epoxy resin and polyvinyl acetate, and found that using the tangent delta methodology to determine the glass transition temperature provided results virtually identical to those obtained from macroscale DMA and DSC.[61] However, nanoindentation is not an ideal technique to probe glass transition of polymers because (1) it generates a complex stress state in the deforming

volume, which includes shear and compressive components that are challenging to calculate, (2) the mechanical response of the material may be obscured by these inhomogeneities in stress and strain, and (3) the boundary conditions of the deforming volume do not include free surfaces, which may not accurately represent deformation of a stand-alone micro- or nano-sized sample.

In this chapter, we develop an approach to microscale glass transition characterization by performing uniaxial compression of cylindrical pillars with a flat punch nanoindenter tip in an *in-situ* nanomechanical instrument. This geometry and experimental setup overcome the limitations of nanoindentation because they allow for unambiguous determination of globally applied stress and homogeneous deformation, *i.e.* they closely resemble macroscale DMA experiments in the compression geometry. However, unlike macroscale instruments, this setup can achieve a stable displacement amplitude of 40nm, which corresponds to 0.25% strain for the 16μm tall pillars. We then apply this dynamic nanomechanical analysis (DnMA) methodology to characterizing the glass transition of the developed candidate shape memory materials.

3.2 Dynamic Nano-Mechanical Analysis (DnMA)

In-situ DnMA data acquisition

We characterized the viscoelastic properties of the synthesized material by performing *in-situ* dynamic nanomechanical analysis (DnMA) experiments inside of an SEM-based nano-mechanical instrument (**Figure 3.1a**) on 8μm diameter pillars (**Figure 3.1b**) by compressing them to 1% strain using a flat punch indenter tip and then applying a 10Hz oscillatory load to generate displacement with a 40nm amplitude.[62] The load profile is illustrated schematically in **Figure 3.1c**, and the representative experimental dynamic response amplitudes are available in **Figure 3.2**. We recorded the amplitude of the load oscillation necessary to maintain this displacement amplitude (166μN at room temperature), as well as the degree offset between the load and displacement waves (2° at room temperature).
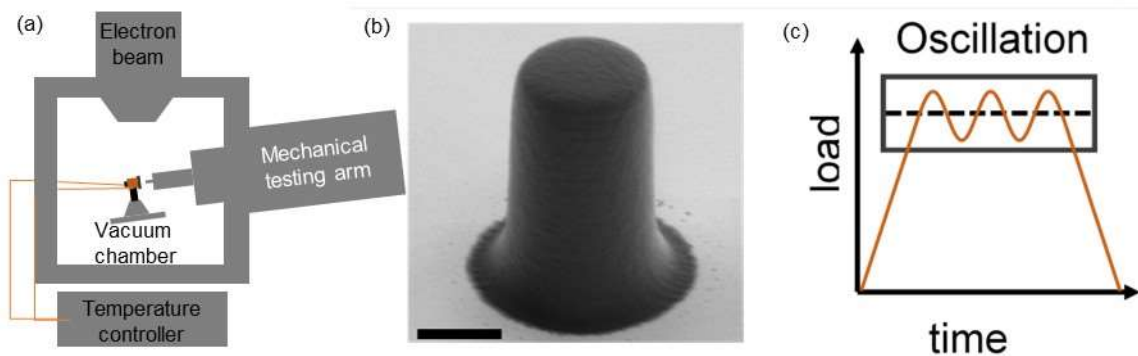
Figure 3.1. Experimental setup for nanomechanical DMA experiments to identify a glass transition. (a) Schematic illustrating *in-situ* SEM sample mounting during mechanical experiments. (b) SEM image of a representative 8µm-diameter cylindrical pillar fabricated for DnMA experiments. Scale bar 5µm, tilt 52⁰. (c) Schematic of the load profile during a typical DnMA experiment. *Adapted from [1].*
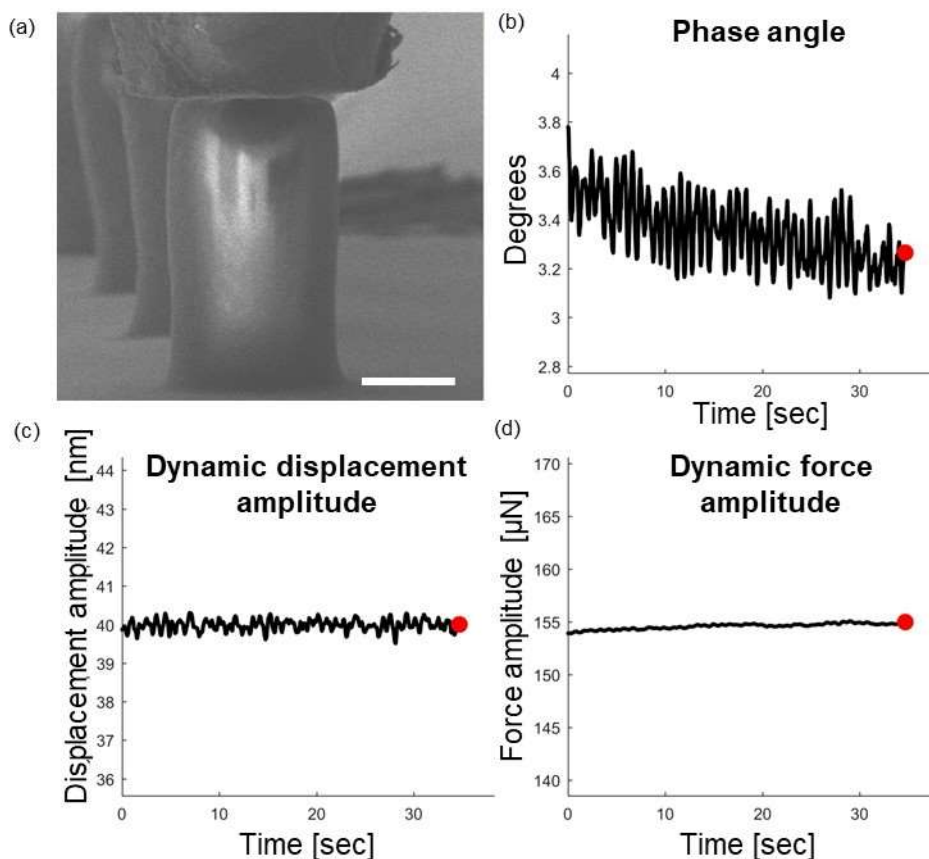
Figure 3.2. Representative data obtained during DnMA experiments. a) Still frame from *in-situ* video acquired during the experiment, displaying the characterized pillar in contact with the nanoindenter flat punch. Scale bar 5µn. Unprocessed phase shift (b), dynamic displacement amplitude (c), and dynamic force amplitude (d) obtained synchronously during the oscillatory portion of the experiment. *Adapted from [1].*

Viscoelastic region

To verify that the DMA experiments were conducted within the viscoelastic region of the material, pillars were loaded to 300µN at a rate of 10 µN/s, held for 10s and unloaded (**Figure 3.3a**). After contact was established, linear loading was observed, followed by unloading with some hysteresis, as is characteristic of a viscoelastic material. During DMA experiments at 40nm target displacement amplitude, the maximum load amplitude observed was 166µN. Therefore, it was expected that the sample would remain within the viscoelastic range and that contact would be maintained. A variety of dynamic displacement amplitudes

were then tested on a series of pillars in 10Hz DMA experiments (**Figure 3.3b-c**).[63] For amplitudes of 50nm and greater, an increase in loss modulus, decreases in storage and loss stiffness, as well as an increase in the tangent delta were observed. For the lower values of 20nm and 40nm, however, these values remained constant, indicating viscoelasticity. The material was therefore determined to be within its viscoelastic region for a pre-compression of 200 µN and a 40nm amplitude 10 Hz DMA experiment.
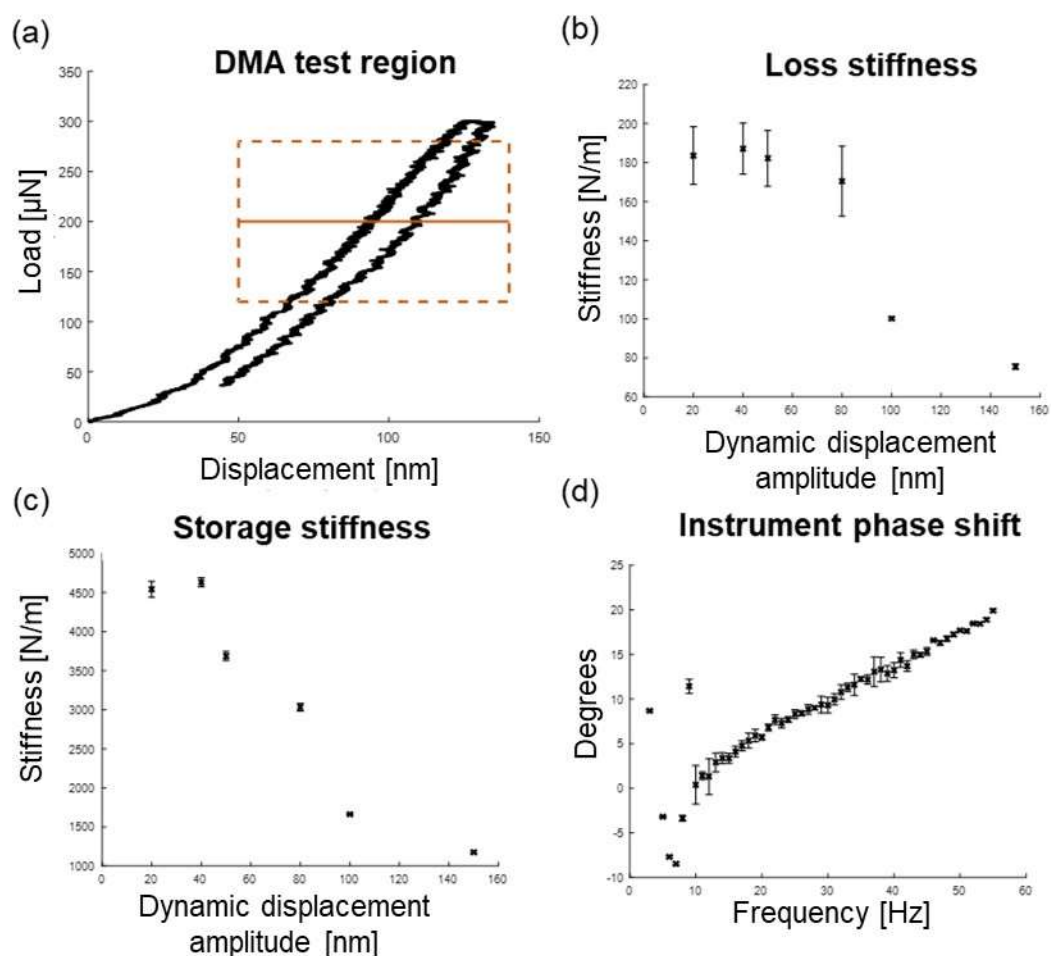
Figure 3.3. Validating DnMA conditions. a) Sample loading/unloading curve for the synthesized pillars at room temperature. The solid line indicates the pre-load used in the DMA experiment, while the dashed box outlines the maximum load amplitude detected during the test. c) Sample loss stiffness determined at various target dynamic displacement amplitudes. Black box correction applied at each target displacement. n=3. d) Sample storage stiffness determined at various target dynamic displacement amplitudes. Black box

correction applied at each target displacement. n=3. d) Instrument phase shift as a function of temperature obtained by oscillating in vacuum. n=3. *Adopted from [1].*

Black box correction

DMA experiments were performed on a nanomechanical instrument that applies force to an indenter column which is supported by springs that restrict motion in one direction. This results in interaction with the sample through a flat punch tip, and a corresponding displacement measured through a capacitive gage. When an oscillatory force is applied, a lock in amplifier is used to isolate the load and displacement signals that occur at the target frequency, allowing the corresponding amplitudes as well as the phase shift to be measured. However, these measured values represent the combined response of the sample and the indenter system. This interaction can be represented by a mechanical model (**Figure 3.4**), allowing the dynamic response of the sample to be isolated from some features of the instrument.[63] In particular, it is expected that both the sample and the support springs will contribute to the measured storage stiffness, while the loss stiffness will be affected by the damping between capacitive plates. They are therefore represented as springs and dashpots, respectively.
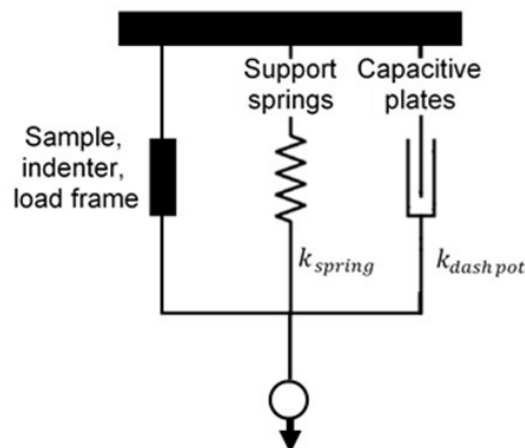
Figure 3.4. Mechanical model of the nanoindentation system. Representative elements are labeled.

The obtained data were corrected to account for these contributions. According to the mechanical model, when the indenter is oscillated in vacuum without contacting the sample, the storage stiffness observed corresponds only to the support springs, while the loss stiffness observed corresponds exclusively to dampening between capacitive plates. The stiffness values representing the sample and its contact with the indenter were therefore calculated as follows:

$$k_{storage} = \left|\frac{F_0}{u_0}\right| \cos(\delta) - \left|\frac{F_0}{u_0}\right|_{vacuum} \cos(\delta_{vacuum}) \qquad (3.2)$$

$$k_{loss} = \left|\frac{F_0}{u_0}\right| \sin(\delta) - \left|\frac{F_0}{u_0}\right|_{vacuum} \sin(\delta_{vacuum}). \qquad (3.3)$$

The calculated stiffnesses correspond to the sample and its contact with the indenter, which are represented by a black box in the mechanical model.[62-64] This indicates that the values obtained do not rely of any assumptions about the mechanical behavior of the sample material. This also means that the response of the sample cannot be decoupled from the contact between the indenter and the material. However, as the polymer sample is significantly less stiff than the diamond indenter, a deviation of under 3% from the true value is expected.[64,61]

To apply this correction, it was first necessary to validate that the indentation system can be described as a one-dimensional oscillator under the target experimental conditions.[63] To do so, the phase angle was measured as a function of frequency in 1Hz increment with the indenter column oscillating in vacuum at the displacement corresponding to the 200μN sample pre-loading (**Figure 3.3d**). Between 10Hz and 55 Hz, no discontinuities were observed, which indicates that at this frequency range, the difference between stiffnesses in the vertical and lateral directions is sufficiently large to prevent cross-talk. Further, the phase angle did not increase past 90 degrees, indicating that the resonant frequency of the instrument was not detected. It was therefore determined that the instrument can be

represented by a one-dimensional oscillator model in the 10-55Hz frequency range, and the black box mechanical model can be applied.

To apply the black box correction, the indenter tip was oscillated in vacuum at the displacement corresponding to the 200 μN sample pre-loading. To analyze both for correction and sample oscillation data, the DMA portion of the experiment was first isolated. That was done by selecting the region where the observed dynamic displacement was within 10% of the target value for at least 1000 consecutive points. The loss stiffness and storage stiffness were then calculated according to Equation 3.2 and Equation 3.3. The ratio between them was then used to determine the corrected tangent delta. At room temperature, applying the correction resulted in a 1% decrease in loss stiffness, 3.9% decrease in storage stiffness, and 2.9% increase in the tangent delta.

The values isolated as a result of this analysis are the stiffnesses of the sample, rather than the moduli of the material. Stiffness is related to modulus by the factor given in equation 3.4 below:

$$\frac{(1-\nu^2)\sqrt{\pi}}{2\beta\sqrt{A}} \tag{3.4}$$

where A and β are geometric factors and ν is the Poison's ratio. Although β and A are known, the Poison's ratio for this material is not. Therefore, stiffness, rather than moduli, are reported and used to track sample properties.

3.3 Temperature-controlled DnMA for glass transition characterization

Black box correction

The oscillation was initially performed after the tip was equilibrated at each target temperature. However, no temperature dependence in the instrument was observed (**Figure 3.5**). Therefore, the correction data obtained at room temperature were utilized for all

experiments. At 87°C, the correction resulted in an 8.8% decrease in storage stiffness, a 0.33% decrease in loss stiffness, and an 8.4% increase in the tangent delta.
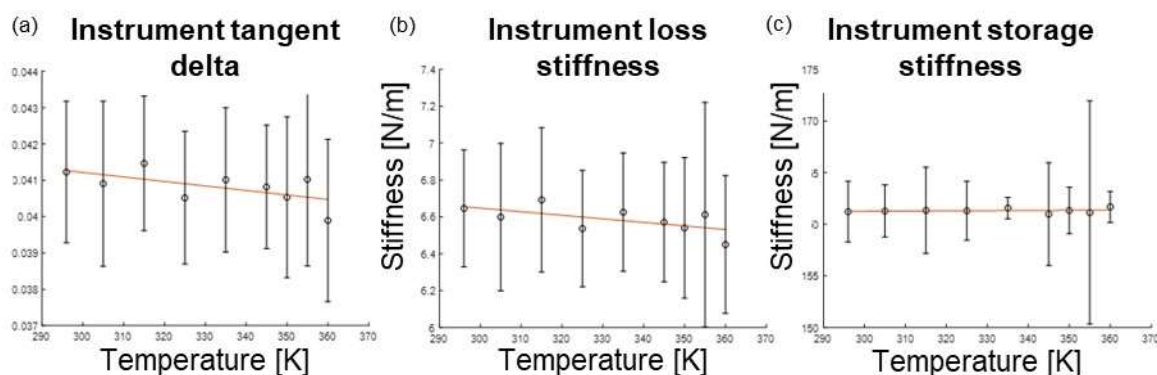
Figure 3.5. Instrument calibration as a function of temperature. Instrument tangent delta (a), loss stiffness (b), and storage stiffness (c) obtained by oscillation in vacuum after nanoindenter tip equilibration at each target temperature. Orange line indicates the line of best fit obtained from linear regression. *Adopted from [1].*

Glass transition characterization

We characterized material temperature dependent dynamic response in step-wise experiments, by raising the temperature in 10°C increments from 22°C to 82°C, with additional data obtained at 78°C and 88°C. We probed pillars of two different materials: one fabricated from the candidate shape memory material (BMA pillars), and the other from the commercial IP-Dip resist (Nanoscribe GmbH), which is a highly crosslinked resin composed primarily of pentaerythritol triacrylate that is routinely used in two photon lithography. The latter is not expected to exhibit glass transition or shape memory properties. Mechanical data shown in **Figure 3.6a** indicate that the storage stiffness of IP-Dip remains within 7% of its RT (or initial) value throughout the temperature range; the benzyl methacrylate samples exhibit a sharp 56% decrease in storage stiffness, from 3,860 +/- 48 N/m at 22°C to 1,700 +/- 140 N/m at 87°C. Similarly, the loss stiffness of the IP-Dip samples remained within 21% of its room temperature value, the loss stiffness of the BMA based pillars peaked at ~ 77°C, a factor of 2.9 increase relative to its room

temperature value (**Figure 3.6b**). The tangent delta of the IP-Dip pillars did not increase significantly, while a factor of 6.5 increase is observed for the BMA sample (**Figure 3.6c**).
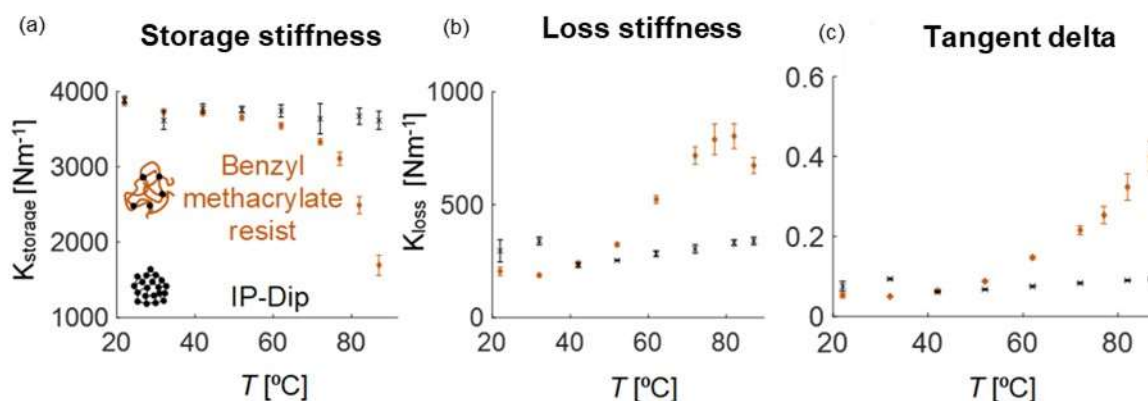
Figure 3.6. DnMA glass transition characterization. Experimentally obtained (a) storage stiffness, (b) loss stiffness, and (c) tangent delta as a function of temperature for samples fabricated from the synthesized benzyl methacrylate-based resist (orange diamonds) and from the standard commercial IP-Dip resist (black crosses). Corrections for instrument stiffness were applied to all data. Error bars represent one standard deviation, n=5. *Adopted from [1].*

Effect of frequency

We explored the influence of frequency on the glass transition characteristics by conducting additional DnMA experiments at 10Hz and 50Hz. As expected from the principle of time-temperature superposition, we observed an increase in the frequency of the DnMA experiment to correlate with a decrease in temperature (**Figure 3.7**). In the 50Hz experiment, the tangent delta at 87°C decreased by 20%, the peak in the loss stiffness shifted to a temperature greater than the experimental limit of 87°C, and the storage stiffness at 87°C increased by 30% compared with 10 Hz. This is consistent with the frequency-dependent glass transitions. The 10Hz frequency utilized in this study is one of the standard frequencies commonly utilized in reporting glass transitions.[1] Based on the loss stiffness peak shift

(**Figure 3.7**), employing a 50Hz test frequency would result in an increase in the reported transition temperature by at least 10°C.
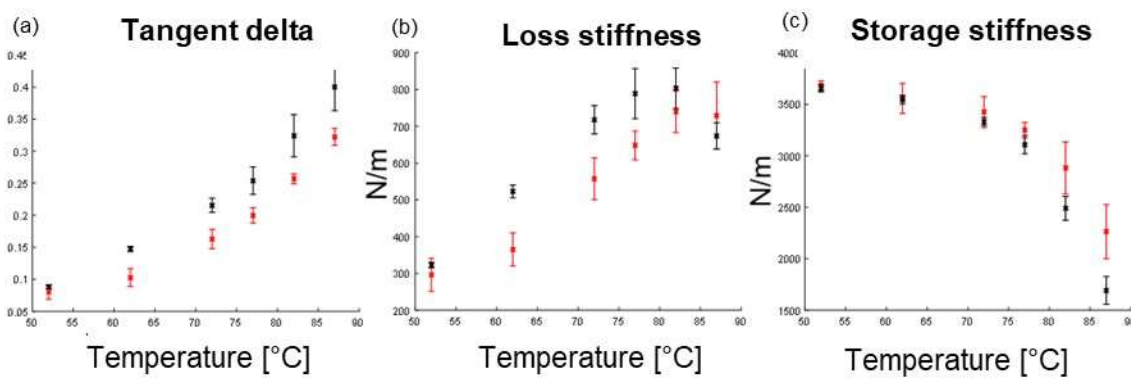
Figure 3.7. Glass transition characterization at varied frequency. Tangent delta (a), loss stiffness (b), and storage stiffness (c) for 8μm diameter pillar characterized at 10Hz (black) and 50Hz (red). *Adopted from [1].*

Effect of crosslinking density

Structures fabricated via TPL-DLW are typically characterized by low conversion, with the degree of crosslinking controlled by laser power and scan speed.[42,65] To probe the effect of crosslinking density on the glass transition, we lowered the laser power during fabrication from 30mW to 20mW while maintaining constant scanning speed and performed DnMA on the produced 8μm diameter pillars (**Figure 3.8**). We observed a broadening in the tangent delta curve and a 10°C shift in the loss stiffness peak to lower temperatures. The storage stiffness decreased from 3, 540 +/- 40 N/m at 62°C to 1, 200 +/- 90 N/m at 62°C. This indicates that a decrease in crosslinking density causes a reduction in stiffness and in the glass transition temperature. The same behavior is expected in macroscale materials.[66]
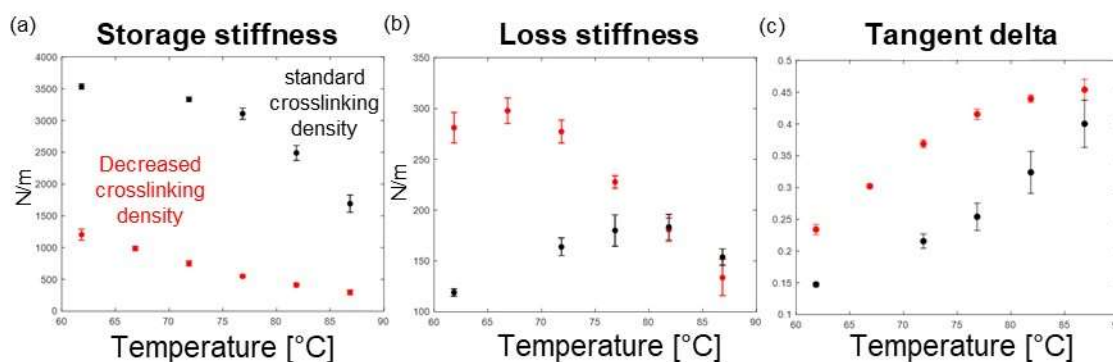
Figure 3.8. Glass transition characterization at varied crosslinking density. Storage stiffness (a), loss stiffness (b), and tangent delta (c) of pillar written at 30mW laser power (black) and 20mW laser power (red). n=5. *Adopted from [1]*.

Effect of sample dimensions

We compared the characteristic DnMA and programming properties of pillars with 8μm and 4.8μm diameters. **Figure 3.9** displays the storage and loss stiffnesses and tangent delta for these samples subjected to 100μN of static load and a 20nm displacement amplitude with the corresponding in-vacuum correction. These results indicate that in the pre-glass transition region, tangent delta and storage stiffness are independent of size. The increased loss modulus suggests increased energy dissipation and the low tangent delta plateau observed at 82°C suggests a broad glass transition region, which is consistent with expected higher heterogeneity and relative contribution of network defects at decreasing scales.
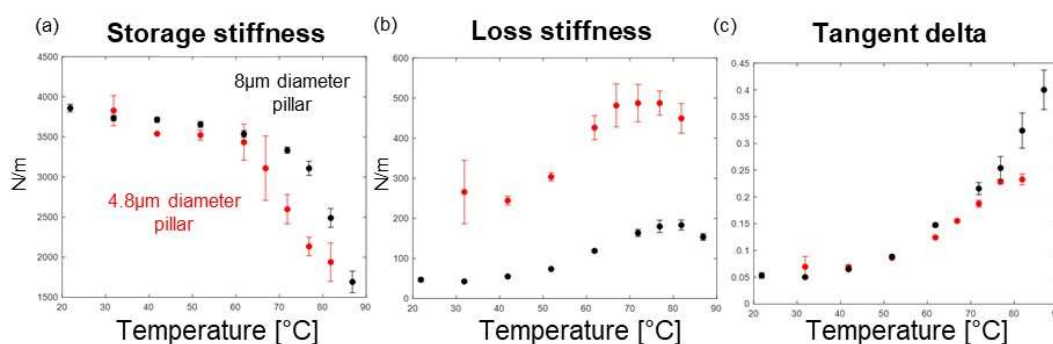
Figure 3.9. Glass transition characterization at varied sample size. Storage stiffness (a),

loss stiffness (b), and tangent delta (c) of 8μm diameter pillars (black, n=5) and 4.8μm diameter pillars (red, n=3). *Adopted from [1].*

3.4 Summary and outlook

We investigated the viscoelastic properties of microscale benzyl methacrylate based polymer networks at the glass transition by performing *in-situ* dynamic nanomechanical analysis of 8μm diameter pillars. To do so, we performed experiments within the viscoelastic region of the material and accounted for the instrument response by adopting the black box correction methodology. We identified a frequency-dependent glass transition region in the benzyl methacrylate based polymer, characterized by a storage stiffness decrease (56%) and a loss stiffness peak (factor of 2.6 increase). This glass transition was not observed in the highly crosslinked commercial IPDIP structures that do not incorporate elastomeric chains, and displayed storage stiffness and loss stiffness within 7% and 21% of room temperature values, respectively. This indicates that the photoresin developed in Chapter 2 was successfully designed to undergo a glass transition through the introduction of monofunctional acrylates, and that provides the glass transition temperature window necessary for optimal shape memory programming.

We then probed the glass transition as a function of tunable fabrication parameters to begin exploring the effects of polymer network architecture on viscoelastic properties. We considered the effects of laser power, which has previously been correlated with crosslinking density, as well as sample size and observed tunable glass transition characteristics. Specifically, decreased crosslinking density (laser power) resulted in a 10°C shift in the loss stiffness peak, while decreasing sample volume by a factor of 4.6 increased the maximum loss stiffness by a factor of ~3. These results indicate that polymer network properties controllable during fabrication can influence the viscoelastic response, and suggest that further studies correlating network characteristics such as local crosslinking density and the number of elastically active chains are necessary. This could be accomplished through solid state ^{1}H NMR T_2 relaxation experiments, since T_2 relaxation

times probed above the glass transition can indicate chain lengths between network junctions.[67]

3.5 Experimental methods

Preliminary in-air room temperature DnMA method

Preliminary room temperature DnMA experiments were performed in air in a nanomechanical instrument (Hysitron Tryboindenter) using a diamond flat punch 8μm diameter tip on 6μm diameter pillars. Samples were pre-loaded to 130 μN at the rate of 10 μN/s. As only dynamic load control could be implemented, a dynamic load amplitude of 100μN was applied at 10Hz for 1 minute. This setup used to verify repeatability of single pillar experiments: stable dynamic modulus of 1690MPa +/- 0.9% was observed in 4 consecutive experiments at room temperature if 15-minute pauses between tests were implemented. Conversely, consecutive experiments resulted in a 5% dynamic modulus increase.

***In-situ* DnMA method**   .

DnMA was performed on an *in-situ* nanomechanical instrument (InSEM; Nanomechanics and FEI Quanta 200) using a diamond flat punch ~12μm diameter tip. Samples were pre-loaded at the rate of 10 μN/s. Unless otherwise noted, DMA experiments were performed at a pre-load of 200μN, at 10Hz and a target dynamic displacement amplitude of 40nm.Video and deformation data were captured simultaneously for representative experiments (**Figure S4**). To achieve stable target dynamic displacement, the method included a one-second pause between static and dynamic loading segments. If a pillar was probed repeatedly due to initial misalignment with the indenter tip, a pause of 15 minutes or more was implemented between experiments to allow for material relaxation.

Temperature control

The temperature was controlled through a resistive heating module located directly underneath the sample mount, a silicon diode on the mount located directly opposite the sample and a PID temperature controller (Lake Shore Cryotonics). The resistive heater is encapsulated in high temperature epoxy and can achieve heating up to 500°C. However, the silicone diode is rated to 100°C and therefore currently limits the temperature range of the instrument. The response of other SEM components to temperatures above 100°C is unknown. The instrument is also equipped with a 'cold finger,' enabling cooling to liquid nitrogen or liquid helium temperatures. This capability was not routinely utilized in the above experiments as it exacerbates drift experienced during temperature transitions.

To equilibrate the sample and erase any previous thermal history and residual stresses, at the initiation of each DnMA experimental sequence the setup was heated to 90°C and allowed to cool to room temperature. The setup was then heated to 90 °C again and equilibrated overnight to minimize temperature fluctuations during compression. For each subsequent descending temperature, the setup was equilibrated for 1h. Before each experiment, the tip was placed in contact with the substrate and allowed to equilibrate for ~30 min to minimize thermal gradients.

Chapter 4

EXPLORING THE PARAMETER SPACE IN SHAPE MEMORY RESPONSE IN MICRO ARCHITECTED POLYMERS

Adapted from:

4.1 Introduction

Characterizing the shape memory response

Polymers can exhibit a thermally driven shape memory effect if deformation above the transition temperature results in conformational changes with minimal energy dissipating chain slippage. This can be achieved by a variety of polymers that consist of netpoints that can store a permanent shape and temperature sensitive mobile segments. The efficiency of this process is typically quantified through shape fixation and shape recovery ratios, which respectively quantify a polymer's ability to maintain a temporary deformation and recover the original structure.

These parameters can be determined through a variety of thermomechanical programming tests: tensile, three-point flexural, compression, or bending. The most widespread approach is cyclical tensile testing. The test begins with a programming module where a sample is deformed and cooled under stress or strain controlled conditions. Recovery can then occur either under stress free-conditions or under constant strain.[68] In stress-controlled programing with stress-free recovery, the shape fixity ration R_f is the amplitude ration of the fixed deformation for an individual programming cycle N and is given by equation 4.1 below.

$$R_f(N) = \frac{\epsilon_u(N)}{\epsilon_l(N)} \qquad (4.1)$$

Here $\epsilon_u(N)$ is the tensile strain after unloading and $\epsilon_l(N)$ is the maximum strain after cooling to T_{low}. The shape recovery ration R_r is the measure of how far strain applied in the course of programming is recovered, as indicated by equation 4.2 below.

$$R_r(N) = \frac{\epsilon_l(N) - \epsilon_p(N)}{\epsilon_l(N) - \epsilon_p(N-1)} \qquad (4.2)$$

Here the strain of a sample in the stress free-state at the initiation of a programming cycle is given by $\epsilon_p(N)$, with the stress at the initiation of the preceding cycle provided by $\epsilon_p(N-1)$. Although the obtained parameters are influenced by deformation and fixation temperatures, as well as heating and cooling rates, at the macroscale they can be precisely determined in a tensile testing machine equipped with a temperature control chamber. [68]

Microscale SMP programming

Thermomechanical programming at the microscale is characterized by methodological difficulties. Ensemble programming has been performed by embedding microscale objects within more easily manipulatable dissolvable macroscale materials, or uniformly compressing arrays of structures.[36,37] These approaches require the separation of programming and characterization steps and provide averages rather characteristics of individual micro structures. Only recently have L. Fang *et al.* developed an AFM-based thermomechanical programming methodology specifically for micro and nanowires capable of deforming and simultaneously characterizing individual structures.[69] In this chapter, we discuss an *in-situ* thermomechanical programming approach to individually quantifying the shape memory response of the fabricated micro structures. We then explore factors that could influence the shape memory response, including crosslinking density and architecture.

4.2 Shape memory response quantification

Shape memory programming cycle

We thermomechanically programmed BMA structures using an *in-situ* temperature-controlled compression experiment (**Figure 4.1a**). Samples of each geometry were first

compressed to 400 µN at 77 ºC using a flat diamond nanoindenter punch and cooled to 42ºC while maintaining the compressive load. The load was then removed, and the samples remained in the compressed configuration for over 30 minutes. Free recovery initiated within one minute of incipient heating; heating the samples to 87ºC at a rate of 10ºC/minute caused them to recover 95% of their original height within 5 minutes. Flower structures displayed a similar response to this thermomechanical programming protocol (**Figure 4.1a**).

The temperatures selected for this programming protocol were informed by prior DnMA characterization (Chapter 3). We chose to program our samples at 77°C, which corresponds to the loss modulus peak. This temperature is expected to be optimal for shape memory programming because the conformational changes of the polymer chains attain their maximum near the peak loss modulus temperature and enable greater stored entropic energy.[59] The storage and loss stiffness *vs*. temperature data (**Figure 3.6a-b**)) also indicates that the SMP is reliably in its glassy state below 42ºC, which guided our choice of 42ºC as the target cold temperature in the programming step of the shape memory cycle.

Cubic lattice shape memory programming

To gain deeper insights into the deformation mechanism, we tracked the vertical displacement of the nodes within the individual facets of cubic lattices relative to the base of the structures at each stage of the programming cycle (**Figure 4.1b**). We measured vertical deformation in excess of 4µm, which corresponds to a global strain of 31%, during mechanical programming and heat induced recovery, with the highest values occurring in the top-most nodes. Displacements of < 1µm (<8% global strain) were evident in the programmed structure prior to heat induced recovery. No net displacements of over 2µm (16% global strain) were detected at the conclusion of the programming cycle.
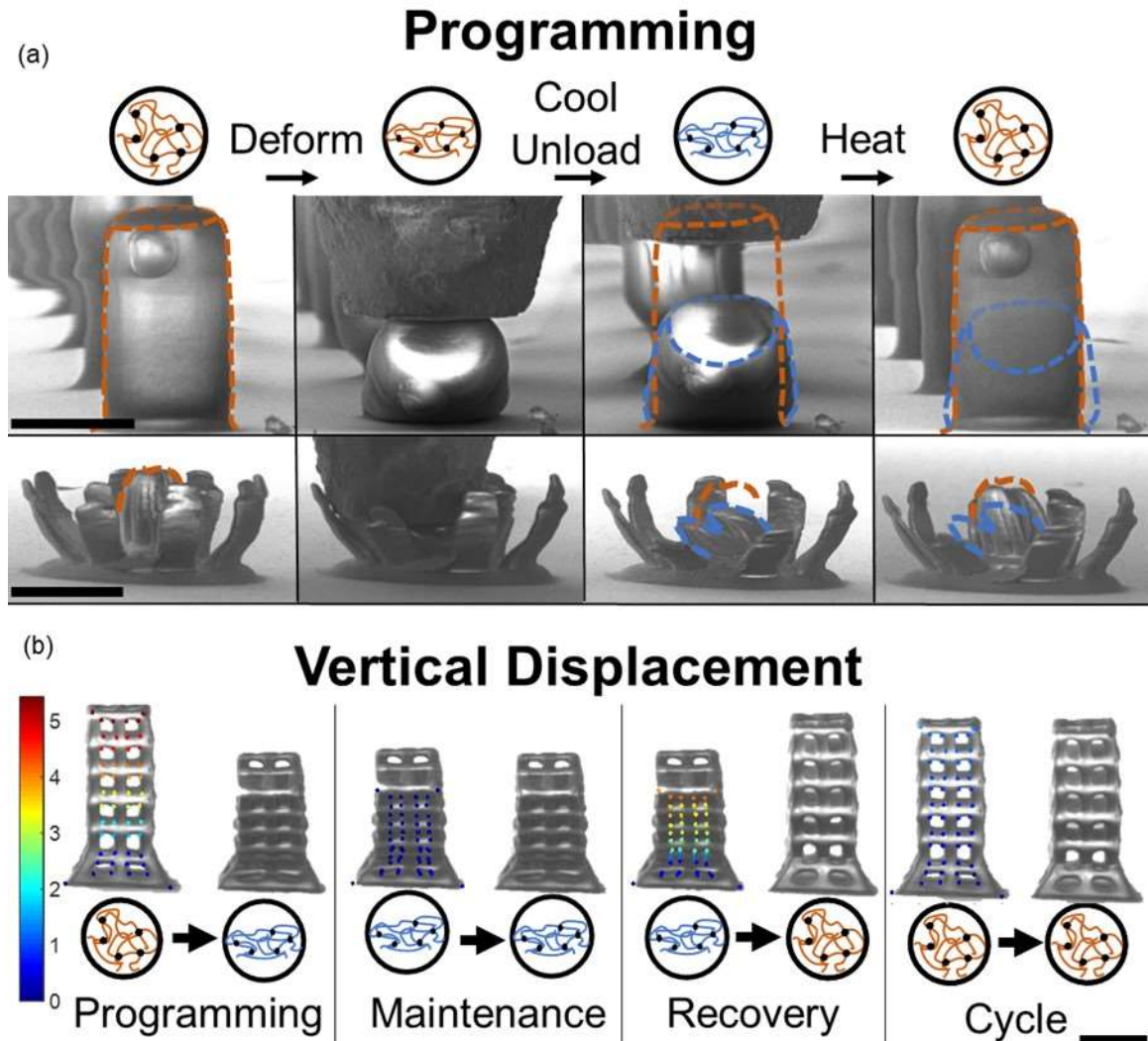
Figure 4.1. Shape memory programming of 3D-architected SMPs. a) A schematic and SEM images of the shape memory programming cycle for a cylinder (top row) and a flower (bottom row): Step 1. Applying a 400µN compressive load at 77ºC, Step 2. Cooling to 42ºC under load, followed by load removal, Step 3. Unconstrained heating to 87ºC to induce shape recovery. Scale bar 10µm. b) Visualization of local vertical displacements within cubic lattices during each step of the programming cycle. Color represents relative displacement of each point of the lattice in µm (left vs. right). Scale bar 5 µm. *Adopted from [1].*

To quantify the observed shape memory effect, we utilized 10µm tall cubic lattice samples subject to the same load-controlled, free recovery conditions. The lattice shape recovery ratio R_r is given by Equation 4.3:

$$R_r = (h_{temporary} - h_{recovered})/(h_{temporary} - h_{original}) \tag{4.3}$$

Here, h represents the bottom-to-top distance of the structure's front facet measured from SEM images. **Figure 4.2** provides an example of the described deformation and displays the height values at the relevant phases of the programming cycle used in the calculation. Using Equation 4.3, we obtain the characteristic shape recovery ratio, R_r of $86 \pm 4\%$. This value is within the 80-99% range expected for macroscale SMPs.[70]
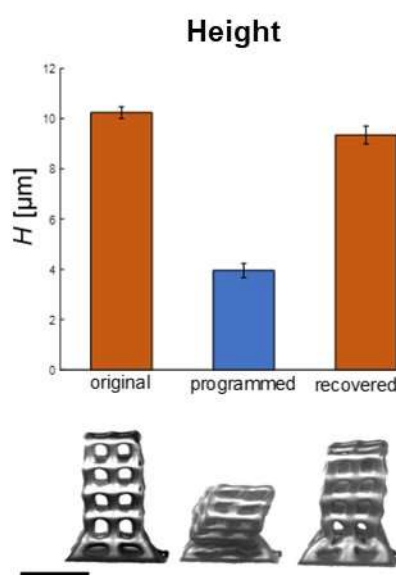
Figure 4.2. Cubic lattice programming quantification. Lattice height in µm before programming, the programmed state, and after recovery, with representative sample image displayed below. Scale bar 5µm. Error bars represent one standard deviation, n=3. *Adopted from [1].*

Alternate programming conditions

We considered two alternate programming conditions: (1) an increase in the final programming temperature from 42°C to 60°C, where the polymer should not reach a glassy state and (2) a decrease in the initial programming temperature from 77°C to 66°C, where the polymer is insufficiently heated below the loss modulus peak temperature. The thermomechanical properties corresponding to these programming parameters are displayed

in **Figure 4.3a-c**, with the corresponding images of cubic lattices throughout salient points of each programming cycle displayed in **Figure 4.3d-e**. These results reveal that at high final programming temperature (**Figure 4.3d**), the structure recovers immediately after the programming step, prior to the application of heat to trigger recovery. Some plastic deformation is observed, likely attributable to lateral drift during programming, and results in a shape recovery ratio of only 8%. In the case of a low initial programming temperature (**Figure 4.3e**), the load applied during programming results in predominantly plastic deformation, as indicated by the broken beam highlighted in the figure, and marginal shape recovery observed upon heating (shape recovery ratio of 7%). These results support the chosen standard programming temperature range of 42°C to 77°C; effective programming requires polymer chain mobility that emerges at the loss stiffness peak at incipient load application and a sufficient reduction in polymer chain mobility at the final programming temperature to prevent recovery following load removal.
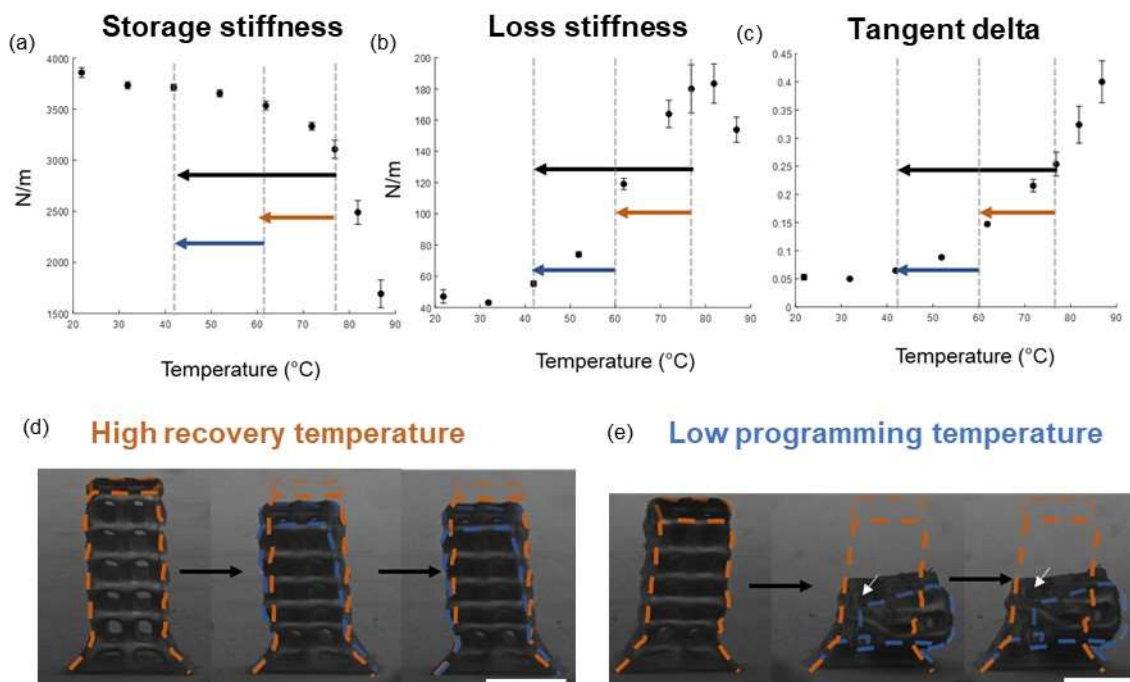
Figure 4.3. Alternate programming conditions. Storage stiffness (a), loss stiffness (b), and tangent delta (c) overlayed with temperature changes during the programming step of the

shape memory cycle. The original temperature change from 77°C to 42°C under load is illustrated with the black arrow. The orange arrow illustrates high final programming temperature — removing the programing load at 60°C rather than 42°C. The blue arrow illustrates low initial programming temperature — beginning programming by applying load at 60°C rather than 77°C. Shape memory effect of 3D lattices programmed (a) at a higher final temperature of 60°C, with load applied at 77°C and removed at 60°C, and (b) at a lower initial programming temperature of 60°C, with load applied at 60°C and removed at 42°C. Dashed orange outline corresponds to the original geometry, dashed blue outline represents the programmed structure. White arrows indicate a broken beam. Scale bar 5μm. *Adopted from [1].*

Alternate structures and characteristics

	Shape fixity	Shape recovery	Recovery time
Cubic lattice	97 +/- 4%	86+/- 4%	174 sec (video S1)
Pillar	80 +/- 30 %	96 +/- 3 %	127 sec (video S2)
Flower	87 +/- 17%	79 +/- 6%	176 sec (video S3)

Table 4.1. Shape memory properties of varied microarchitectures.

Shape memory properties of samples with three geometries (lattice, pillar, and flower) were characterized through the shape recovery ratio (Equation 4.3) as well as the shape fixity ratio given by equation 4.4 below

$$R_f = h_{temporary} / h_{programming} \tag{4.4}$$

where h represents the bottom-to-top distance of the structure's front facet measured from SEM images. The shape recovery time was also recorded (**Table 4.1**). The *in-situ* programming conditions are most conducive to quantifying shape recovery in cubic lattices and pillars. The following limitations apply to other parameters and structures:

1) Determining the shape fixity values requires quantifying total deformation i.e. the deformation during the programming step while the sample is in contact with the indenter. To approximate this value, we utilized the distance between the edge of the indenter tip and the base of the sample. Obstruction of the full sample view by the

indenter tip is a possible source of error that could be causing the substantial standard deviation.

2) The measured recovery times are influenced by the experimental setup because the sample is not immediately heated to the target recovery temperature. Heating during recovery occurs at the maximum rate allowed by the instrument (10°C/min), and the reported recovery time reflects the combined material response over this evolving temperature profile.

3) We isolated vertical deformation to determine the shape fixity and recovery ratios for cubic lattices and pillars; the appropriate deformation metric for more complex structures, such as a flower, is less clear. We chose to track the bending angle of a set of petals as the representative parameter.

Thermal drift

The error observed in this quantification, as well as the incomplete recovery illustrated in **Figure 4.1**, likely stems from the inevitable thermal drift during temperature transitions in the *in-situ* instrument. The cooling portion of the thermodynamic programming cycle requires the indenter tip to be in contact with the sample during temperature changes, which caused the sample to drift laterally by as much as 25nm/ sec. During the ~30 minutes of cooling from 77⁰C to 42⁰C, we observed a net drift of 2μm as indicated by a silicon diode mounted to the sample stage, which introduced inhomogeneities in the stress state of the sample as the material approached its glassy state and likely caused, in part, incomplete sample recovery (**Figure 4.1**). To minimize the adverse effects of the lateral displacement drift, we chose to track the vertical displacement of the sample-tip system, which offers better control and is robust against thermal drift.

4.3 Shape memory response tunability

Effects of crosslinking density

Using these DnMA results as a guide (**Figure 3.8**), we chose to program the structures with a lower crosslinking density at 67°C. Images from a representative programming sequence are displayed in **Figure 4.4**, where the orange dashed outline represents the as-printed structure, and the blue one the programmed configuration. These images display less bending in the pillars during deformation compared with structures printed at higher laser power and programmed at their loss modulus peak temperature (77°C), most probably because the lower programming temperature minimizes lateral stage displacement drift in the instrument. The programmed structures had a characteristic shape recovery ratio of 94 +/- 1%, slightly below that of 96 +/- 3% observed for the high crosslinking density pillars The recovery time (**Video S4**) of 219 seconds exhibited by the lower density samples represents a ~37% increase from the 160 +/- 20 seconds average recovery time for all structures with higher crosslinking density. Both observations are consistent with macroscale free recovery trends in acrylate networks and illustrate the role of crosslinks in driving shape recovery, i.e. increased shape recovery time and lower shape recovery ratio are caused by decreased crosslinking.[66]
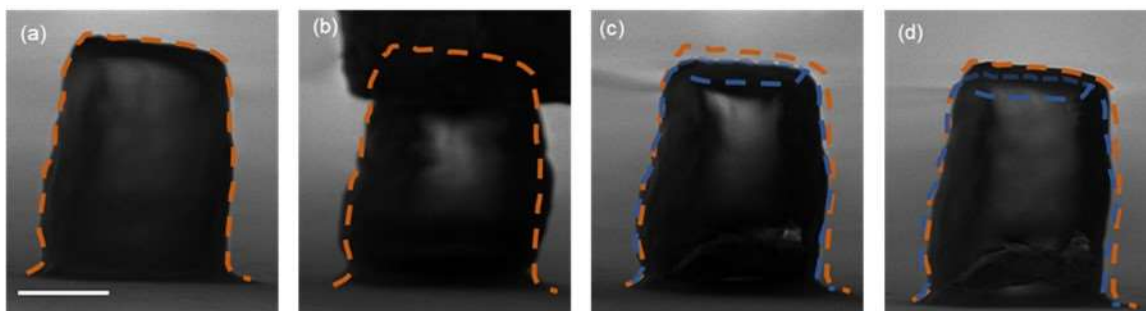
Figure 4.4. Representative shape memory programming sequence for samples fabricated at reduced laser power (crosslinking density). (a) A representative as-printed pillar, (b) initial contact with the indenter tip during programming at 67°C, (c) programmed pillar at 42°C, and (d) after recovery at 87 °C. Orange dashed line outlines the original geometry, blue outline represents programmed state. Scale bar 5μm. *Adopted from [1].*

Effects of structure size

The effects of structure size on shape memory programming are demonstrated through representative images in **Figure 4.5a-b**, which displays a characteristic shape memory programming sequences of the samples. A 14% reduction in the shape recovery ratio with size, from the 96 +/- 3% for the 8 µm-diameter pillars to 82% for the 4.8µm dimeter pillar in **Figure 4.5b** is consistent with the greater degree of heterogeneity within the polymer network observed through the thermomechanical properties (**Figure 3.9**), because regions of high crosslinking density may not contain flexible chains capable of storing entropic energy. We did not observe significant differences in the recovery speed between samples of different diameters (**Videos S5** and **S2**): 159 seconds for the 4.8µm diameter pillars and 127 seconds for 8µm diameter ones. This indicates that in this experimental setup, the recovery rates may be limited by the heating rate of the sample holder rather than by the volume of the microscale sample.
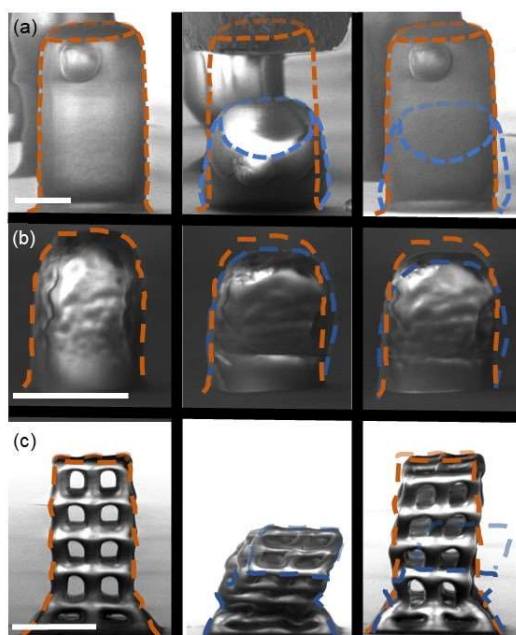
Figure 4.5. Shape memory programing of structures with varied size and geometry. Programming sequence of (a) an 8µm diameter pillar, (b) a 4.8µm-diameter pillar, and (c) a cubic lattice whose solid material volume is equivalent to that of the 4.8um diameter pillar.

Image panels correspond to the initial (leftmost), programmed (middle), and recovered (rightmost) states. Outlines of the original structures are provided in orange and outlines of the programmed shapes are provided in blue. Scale bar 5μm in all structures. *Adopted from [1].*

Effects of structure geometry

We also explored the effect of structure on shape memory response (**Figure 4.5b-c**). We estimated the volume of the 4.8μm cylindrical pillars to be 114 μm^3 and matched it to the material volume of ~119 μm^3 for the cubic lattices, estimated from CAD geometries and SEM images. Any variability in shape recovery between these two types of samples would then be attributed to the geometry, i.e. the >3x greater surface area and a 6x lower minimal feature size in the lattices. The observed shape recovery ratio of 82% for the 4.8μm pillar is within the 86 +/- 4% range observed for cubic lattices, rendering geometric variability inconsequential for shape recovery. This suggests that in this size regime, the variability in the polymer free surface glass transition does not play a major role in shape recovery and that characterization performed on pillars can be used to determine the behavior of more complex structures.[71]

4.4 Summary and outlook

In this chapter, we utilize the shape memory structures designed and fabricated in Chapter 2, as well as the understanding of their thermomechanical properties gained through the dynamic mechanical characterization described in Chapter 3, to demonstrate shape memory programming of architected materials at the microscale. The *in-situ* thermo-nanomechanical programming cycles demonstrate a glass transition-based shape memory effect on isolated micro-architectures with different geometries, including pillars, cubic lattices, and flowers, with a shape recovery ratio of $86 \pm 4\%$. These results may have significant impact on a broad range of technologies that require small-scale temperature-induced shape re-configurations, ranging from miniaturized deployable biomedical devices, such as stents for retinal vasculature to stimuli responsive mechanical metamaterials.

The shape memory mechanism described here could interact with other effects prevalent in microfabricated structures. For example, precise control over the degree of conversion available through variable laser writing trajectories could be used to develop single material structures with regions that undergo glass transitions at varied temperatures.[72, 73] This would result in more complex shape recovery trajectories, as portions of the structure would recover sequentially during temperature increases.[3] Further, shape memory could be combined with residual stress induce shape changes for more rapid fabrication of responsive structures. Residual stresses present due to polymerization-induced shrinkage can be used to induce self-bending, which converts planar structures to 3D during development.[74] These structures could be shape memory programmed, with any contribution from remaining residual stresses minimized through heating prior to the thermomechanical programming.

4.5 Experimental methods

Sample mounting

Samples were typically mounted to the heated stage with colloidal graphite. Alternative mounting methods included silver paint, high temperature epoxy, and high temperature carbon paste, and did not results in reduced drift during cooling.

Equilibration

Samples were heated within the SEM chamber to 90º C, allowed to cool to room temperature, and then heated to the target programming temperature and equilibrated for 1 hour. The indenter tip was placed in contact with the substrate for 30 min by maintaining a constant 20μN load in response to drift driven vertical stage displacement.

Programming and recovery

The sample was compressed to 400μN and the load was maintained for 10 min, after which heating was turned off. The sample was allowed to cool to the target temperature while the

static load was maintained with the indenter compensating for any vertical drift induced displacement. Still SEM images were captured during programming, immediately upon unloading, and prior to the initiation of heating. To trigger shape recovery after at least 30 minutes at the target cooling temperature, the setup was heated to 87 ºC, with video or still SEM images captured throughout.

C h a p t e r   5

APPLICATION: DEEP BRAIN NEURAL PROBE DELIVERY

5.1 Introduction

Long-term neural recording in large scale brains

Long-term neural record has exciting applications in areas such as neuroprosthetics, brain mapping, brain-machine interface and investigation of neurological disorders. [20] These technologies can benefit greatly if recording capability is transitioned from mouse models to larger scale brains, enabling applications in primates and eventually humans. The transition requires the ability to deliver long-term recording devices to precise areas located centimeters deep within the brain while inducing minimal damage.[75] A successful insertion device will fulfill several recording goals, which translate to design requirements as described below:

Accurate targeting: Most current probe placement approaches have been developed for rodents, where targeting requirements are moderate. "Deep" brain areas in a rat (e.g. hippocampus) require only accurate targeting within a 5 mm diameter at a 5 mm depth.[76,77] In contrast, with larger animals such as macaques, the accurate targeting of functionally identified deep brain areas, ~2 mm diameter and 30 mm deep, presents a significantly more challenging problem, and requires angular deviations of less than 2 degrees.[72]

Uninhibited long-term recording: Acute tissue damage during probe insertion is a function of probe cross-sectional area, where larger probes produce foreign body response 'dead zones' that inhibit recording.[78] The diameter of the state-of-the art commercial brush array electrode used in monkey surgeries is 350-665μm, depending on the desired number of electrodes.[79] While a minimum diameter is desirable, a diameter of ~ 100-300μm is comparable to accepted rodent implants. Long-term recording is further inhibited by encapsulation, which is correlated to high probe stiffness and density due to inertial effects and stress at the tissue-implant interface during respiratory and cardiac micromotions.[80] To

minimize these effects, the implant properties should approach tissue density ($\rho = 0.99$ g/cm^3) and stiffness (E=0.5-1kPa).

Usability: For successful integration into existing primate surgical procedures, the probe should maintain the mechanical properties necessary for maneuverability and repeated insertions for 6 hours, which is the maximum duration of surgery based on safe anesthesia times. It should be compatible with existing placement guides that enable brain region targeting based in fMRI data, which require a total probe length of >84mm.[75] It should also enable placement visualization via MRI.

Architected shape memory materials for neural recording

Shape memory materials provide a number of advantages in deep brain electrode delivery. Shape memory-based recovery in response to body temperature can serve as deployment mechanism, moving the electrode away from the site of initial insertion damage.[22] Tissue damage during this secondary insertion can be minimized through tuning the recovery rate to match neuron migration rates, which range from ~0.7μm/min for immature neurons migrating through the adult brain to ~ 1μm/min for microglia migration.[22] SMPs can also be used to reduce the modulus mismatch between the device and surrounding tissue. Specifically, plasticization of SMPs with water lowers the glass transition post-implantation due to swelling-induced increase in free volume.[81,82] Since SMPs are characterized by a large stiffness differential between the glassy and rubbery state, the post-implantation modulus can be reduced by over 2 orders of magnitude, as demonstrated by thiol-ene based electrode storage moduli decreasing from ~500MPa to ~15MPa.[83]

Introducing microscale architecture to these materials could further improve long term recording capabilities. Deployment of architected structures can enhance the stiffness differential observed post implantation. Cubic lattices undergo beam buckling during compression, after which stiffness of the fully dense structure is largely determined by the constituent material. It follows that recovery of lattices implanted in the compressed

configuration will result in a decrease in structural stiffness as the buckling deformation mode becomes available. Architecture can also be used to establish an optimal recording site. Neural tissue engineering studies suggest that pores in the range of 20-160 μm are optimal for supporting 3D cell-to-cell contacts, facilitating mass transport, and enabling the formation of micro-vessels.[23] Deploying electrodes within such scaffolds should facilitate an optimal long term recording environment.

Neural electrode delivery to deep brain recording sites

Deploying neural electrodes with architected shape memory polymers for deep brain recording requires the surgical implantation of these electrodes. In large scale brains, effective implantation to the target 30mm depth of electrodes with minimal cross sectional area is primarily limited by buckling, which can result in off-target electrode placement. Buckling of an Euler beam, which can be used as an idealization that represents the neural implant, occurs when the insertion load exceeds the critical buckling load of the structure, given by equation 5.1 below:

$$P_{crit} = \frac{\pi^2 EI}{(KL)^2}.$$

(5.1)

Here E is the elastic modulus of the material, L is the unsupported beam length, and K is the column effective length factor, which, if we assume that the probe is fixed at the base and free at the tip, is equal to 2. I is the moment of inertia, which for a cylindrical probe is given by equation 5.2 below:

$$I = \frac{\pi r^4}{4}$$

(5.2)

where r is the radius of the probe. As the target insertion depth increases, so does the unsupported beam length, which results in the critical load decreasing proportionally to the square of the length. Further, increased insertion depth results in increasing insertion loads, as illustrated in a representative load-insertion curve for lamb brain tissue provided in **Figure**

5.1a, increasing the critical buckling load required for successful insertion. These two factors dramatically increase the cross sectional areas and/or elastic moduli necessary for successful deep brain insertion, as illustrated in **Figure 5.1b.** This plot provides the theoretical critical buckling load as a function of diameter for cylindrical probes fabricated from materials ranging from polyimide (E=2.5GPa) to tungsten (E=400GPa). The dashed line indicates the expected load during insertion based on linear extrapolation from post-penetration load increases as a function of diameter for cylindrical tungsten probes.[84] The intersection of critical buckling and expected insertion load plots suggest that successful deep brain insertion of probes less stiff than silicon (E=127GPa) with sub 300μm diameters is not likely. As the stiffest shape memory polymers developed for bone scaffolding applications do not exceed 3GPa in the glassy state,[85] shape memory polymers currently cannot be deployed directly to position electrodes in large scale brains.

In this chapter, we therefore focus on the development of a delivery platform that will enable positioning of microscale SMP components at the site of secondary deployment within large scale brains. Rather than controlling the critical buckling load curve through material or geometry selection, we focused on reducing maximum load experienced during insertion. Specifically, we explore the impact of friction on maximum insertion loads during centimeter scale insertions and apply a low-friction coating to minimize its contribution. We validate the low friction probe design in a porcine surgical model, enabling the future development of minimally stiff, low footprint delivery devices.
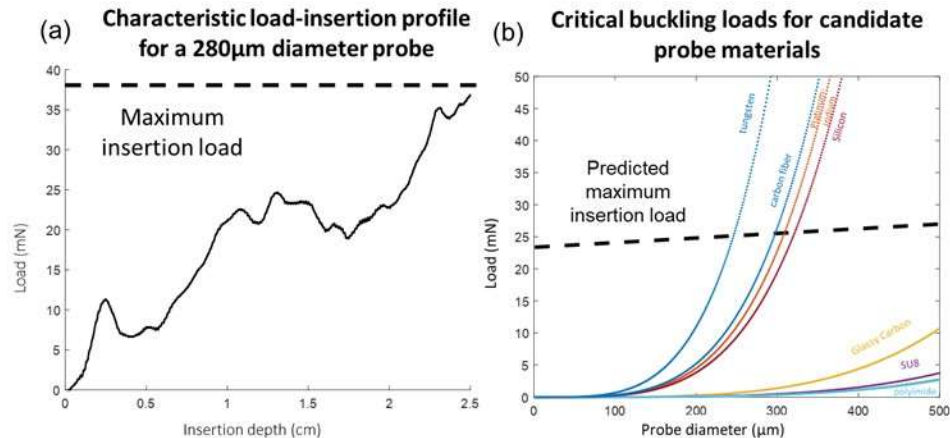
Figure 5.1. Maximum loading and buckling for centimeter scale neural probe insertion. (a) A representative load displacement curve measured for a 280µm diameter probe insertion into porcine brain. (b) Calculated critical buckling loads for a variety of materials as a function of diameter given 84cm length cylindrical geometries. Predicted maximum insertion load for each diameter based on mm scale data from [81] indicated in black for comparison.

5.2 Delivery device design

Carbon fiber probe core

Geometry	Materials	Cross-sectional area (mm²)	Moduli (GPa)	Density (g/ml)	Critical buckling load (mN)
Cylinder	Silicon & platinum iridium	0.0921	73 & 185	15.2	148
Hollow cylinder	Tungsten	0.162	400	15.5	2,200
Cylinder	Tungsten	0.0616	400	19.3	331
Cylinder	Carbon fiber	0.0616	190	7.85	108

Table 5.1. Candidate materials and geometries for neural probe insertion.

A variety of materials and geometries were considered as probe delivery vehicles for 3cm insertions, with candidates described in table 5.1. The silicon and platinum iridium cylinder probe is the commercially available candidate currently successfully inserted into primate brains. Utilizing instead a 280µm diameter tungsten wire would decrease the cross sectional area by 33% while maintaining a critical buckling load above the commercial device.

However, the density would increase by 27%. Converting to the smallest hollow tube tungsten geometry accessible via chemical vapor deposition would maintain a density consistent with the commercial device (2% increase) but would require a 176% increase in cross-sectional area. Utilizing a carbon fiber core with a 280μm diameter would also decrease the cross sectional area by 33%, as well as reduce the probe density by 49%. As the critical load for a 30mm insertion of 230μm diameter device is not expected to exceed 100mN, the carbon fiber core was adopted as the delivery device.

Friction reduction through coating

One mechanism of low sliding friction between surfaces in aqueous media is hydration lubrication, in which hydration shells strongly bound to charges act as boundary layers between surfaces.[86] This mechanism accounts for friction reduction in biological systems such as articular cartilage (friction coefficient of 10^{-3}).[87] One functional group useful in generating these lubricating layers is phosphoryl choline, which is a zwitter ion. Both the –$N(CH_3)_3$ and -CH_2 portions of the headgroup interact with water through hydrogen bonding. Further, the P=O oxygen interacts with on average 2.5 water molecules.[88] A one-pot process under biocompatible reaction conditions has recently been developed for grafting phosphoryl choline containing acrylates onto a variety of surfaces through co-polymerization with polydopamine.[89] Although the precise mechanism of dopamine polymerization is under debate, the oxidative process generates radicals that trigger the free radical polymerization of 2-methacryloyloxyethyl phosphorylcholine. This results in co-deposition of ~24nm films on a variety of plasma activated surfaces and a 0.02 coefficient of friction.[89] This facile deposition process was adopted for friction reduction at the brain- neural probe interface.

Probe fabrication

A carbon fiber based prototype probe was fabricated to identify the role of friction in deep brain insertion. The probe was composed of a carbon fiber rod sputter coated with platinum (**Figure 5.2a**). To evaluate the effect of friction on probe insertion, it was coated with

polydopamine-methacryloyloethyl phosphorylcholine (PDA-MPCP). The coating was applied through a co-polymerization of dopamine and methacryloyethyl phosphoryl choline (**Figure 5.2b**). The successful formation of this coating was verified through Raman spectroscopy. **Figure 5.2c** displays spectra obtained from coated and uncoated samples, with the band at 1457 cm^{-1} corresponding the CH_2 and CH_3 groups of methacryloylyethyl phosphoryl choline and the band at 1594 cm^{-1} attributable to the H-N-C bending vibration of polydopamine.[90,91] The final fabricated rod is 84mm in length, with a 280μm carbon fiber core, a 10nm platinum layer, and a ~100nm PDA-MPCP layer, as indicated by ellipsometry (**Figure 5.2d**).

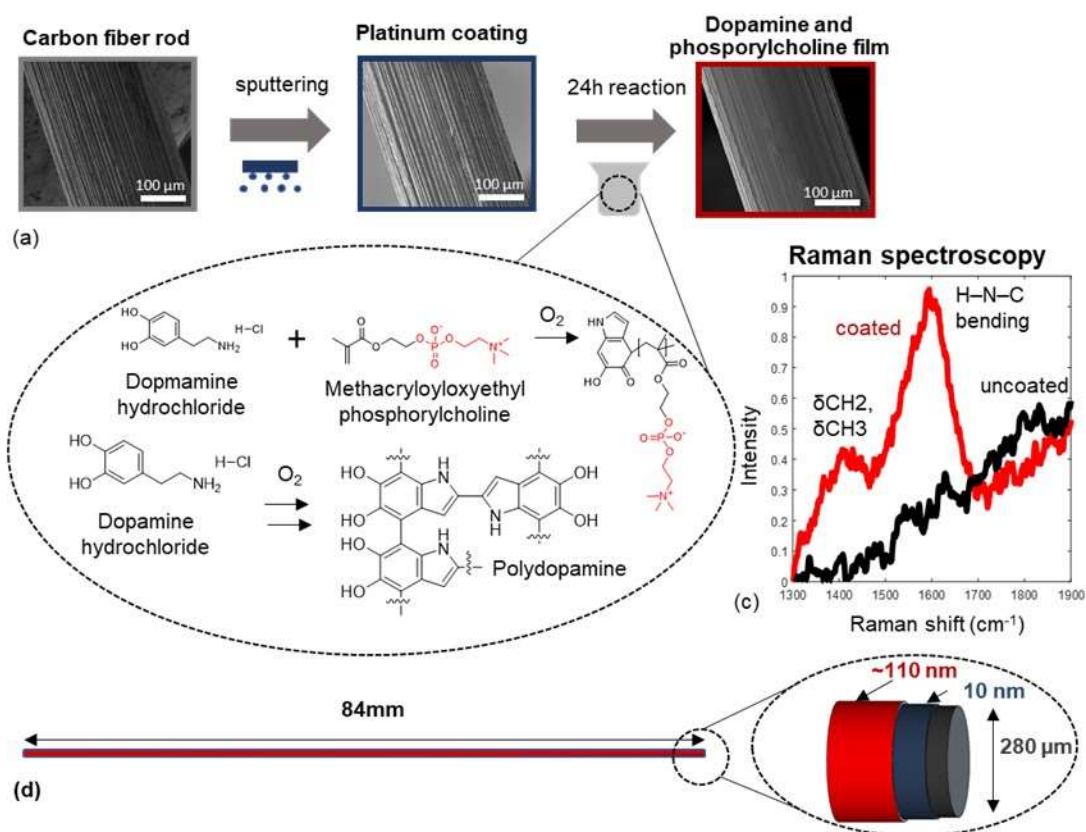**Figure 5.2.** Probe fabrication and characterization A) SEM images of the probe at various stages of the fabrication process: the original carbon fiber rod, the rod after sputter coating with platinum and the rod following coating with polydopamine and polymethacryloyloxyethyl phosphoryl choline (PDA-MPCP). B) Schematic of the oxygen activated PDA-MPCP polymerization. Phosphoryl choline groups are highlighted in red. C)

Raman spectrum of the PDA-MPCP coating on platinum coated glass. D) Schematic of the fabricated rod, illustrating the carbon fiber core, platinum coating, and PDA-MPCP coating. Not drawn to scale.

5.3 Role of friction in neural probe delivery

The role of friction in neural probe delivery was explored using a custom experimental setup, where the fabricated probe was mounted to a load cell positioned on a precision linear stage and inserted into a lamb brain lobe through an insertion guide grid (**Figure 5.3a**). A displacement controlled insertion of the platinum coated probe without the PDA-MPCP coating consisted of three phases: i) penetration, where the probe traveled through the entirety of a lamb brain lobe, ii) puncture, where the probe punctures through the dura membrane on the opposite side of the lobe, and iii) sliding, where the probe interacted with the brain surface without penetrating through any additional tissue (**Figure 5.3b**). These phases can be clearly distinguished on the load displacement curve obtained (**Figure 5.3c**). The initial portion of the loading curve displays a gradual load increase of 5mN intersperse with peaks throughout. The subsequent portion contains sudden load increase of over 20mN followed by detector instability. The final portion of the curve is characterized by a gradual load increase of 7mN without peaks. These regions correspond to the penetration, puncture, and sliding portions of the experiment where cutting and friction, membrane puncture, and friction only forces are recorded, respectively. As the probe interacts with the same brain tissue during the sliding and the penetration portions of the experiment, the contribution of friction during penetration can be isolated despite tissue heterogeneity.
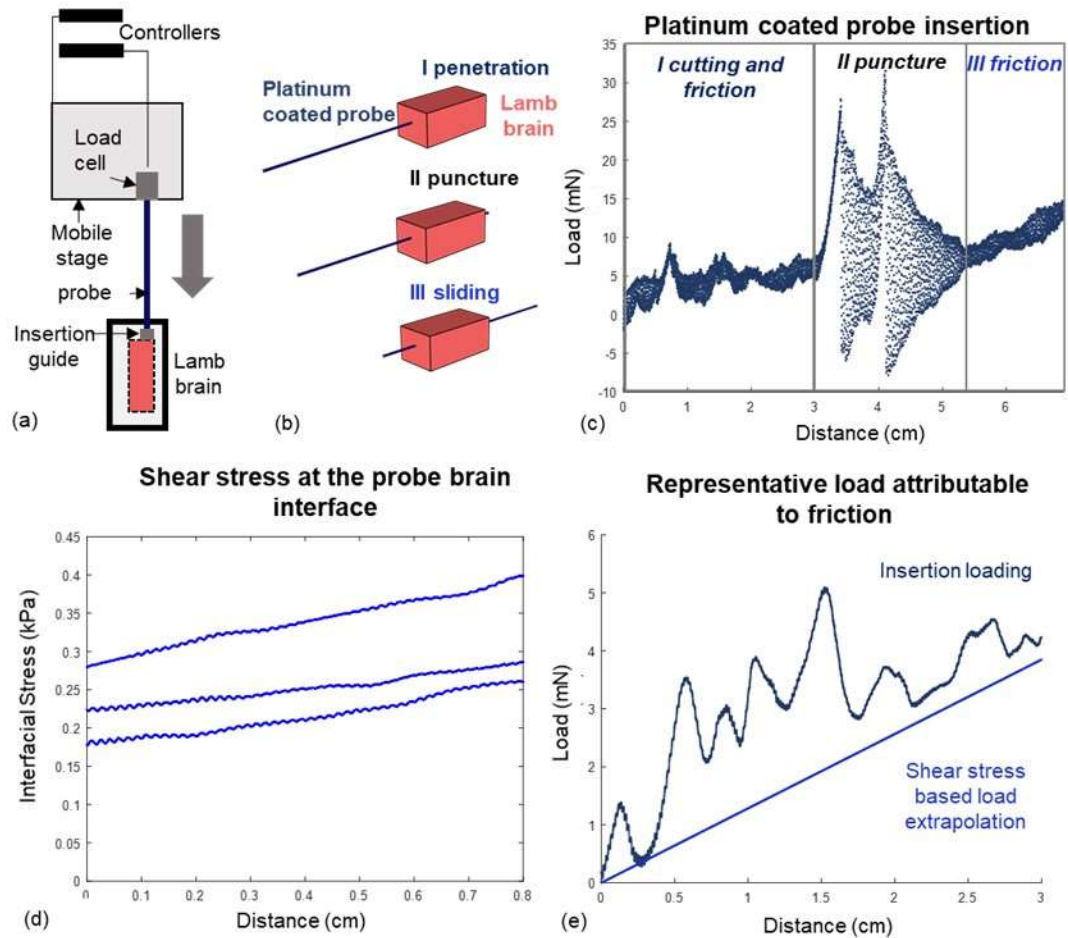
Figure 5.3. Isolating the contribution of friction to loading during probe insertion. A) Schematic of the experimental setup, demonstrating the insertion of the probe into a lamb brain lobe *via* a precision liner stage with load cell monitoring. Not drawn to scale. B) Schematic of the phases of probe insertion into lamb brain: i) penetration of the probe through the whole brain volume; ii) puncture of the outer brain membrane; iii) further sliding of the probe after full penetration through the brain. C) Load displacement curve for a platinum coated probe recorded during the three phases of insertion. D) Interfacial shear stress at the probe brain interface calculated based on probe geometry, insertion depth, and load attributable to friction during the sliding portion of the loading curve. E) Load displacement curve during probe penetration overlayed with the load expected due to friction based on shear stress.

Shear stress calculations

Interfacial shear stress at the brain interface during the sliding portion of the experiment was calculated by dividing the applied load (F) by the contact area between the probe and the brain, as indicated in equation 5.3 below:

$$\tau = \frac{F}{2\pi r L}$$
(5.3)

where r is the radius of the probe and L is the length of the probe interacting with brain tissue, as determined by the difference between insertion depth at initial tissue penetration and tissue puncture. The shear stresses calculated at varied displacement during sliding are shown in **Figure 5.3d**, with the continued linear increase likely attributable to interaction with increasing proportions of a newly wetted probe surface area. As expected, insertions at varied interaction lengths resulted in consistent shear stress determinations (**Figure 5.4**).

Figure 5.4. Shear stress during sliding at varied tissue interaction volumes. A) Axial load measured during platinum-coated probe sliding in various size lamb brain tissue samples. B) Shear stress at the probe brain interface calculated based on axial loading, probe geometry, and tissue interaction length.
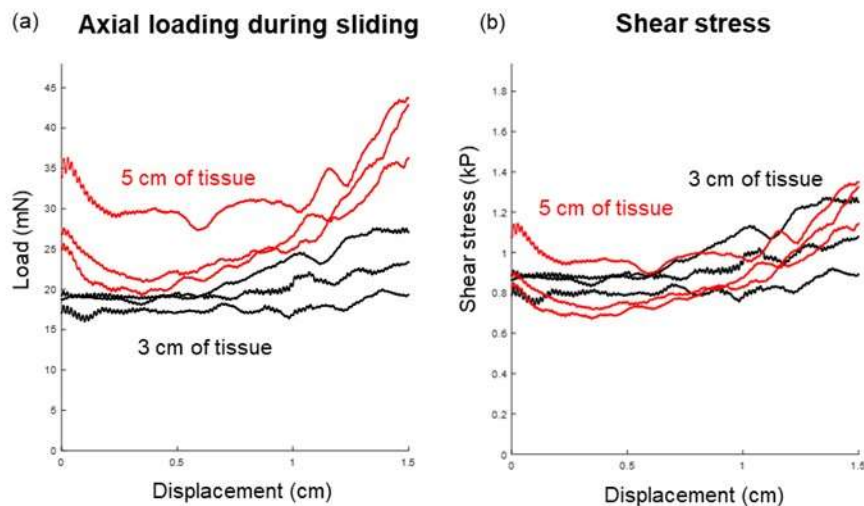
Work attributable to friction

The shear stress calculated during sliding was used to extrapolate the force due to friction expected at the reduced interaction lengths during the initial insertion portion of the experiment. A representative calculated load is overlayed with the recorded penetration loading in **Figure 5.3e** and suggests that, while periodic peaks during insertion can be attributed to tissue heterogeneity and internal membrane puncture during tissue cutting, the underlining linear trend is due to friction. Integrating the areas below the two curves indicates that 59 +/- 3% of work during the 3cm insertion is attributable to friction. This demonstrates that friction reduction is a viable approach to minimizing loading during centimeter scale neural probe insertions.

5.4 Minimizing friction for deep brain insertion

Friction reduction

To determine the role of probe surface coating in minimizing the shear stress at the brain interface, an alternate probe configuration was fabricated, containing an uncoated carbon fiber section, an oxygen activated platinum section, and a PDA-MPCP coated region (**Figure 5.5a**). The rod was fully inserted into the lamb brain lobe, such that no tissue puncture occurred during the various portions on the experiment, where the carbon fiber, platinum, and PDA-MPCP regions on the probe interacted with the same brain region (**Figure 5.5b**). Shear stress was calculated based on load recorded during each of these sliding experiments (**Figure 5.5c**), with carbon fiber samples demonstrating the highest stress (1.3-2.4kPa), platinum demonstrating an intermediate stress range (0.5- 0.9kPa), and PDA-MPCP coating demonstrating the lowest stress (0.5-0.6kPa), resulting in a 20 +/- 7% shear stress decrease for the PDA-MPCA coating as compared to platinum. The uncoated carbon fiber portion of the rod displayed increasing stress (63% increase) and variable peaks during sliding displacement. Both the platinum coated and PDA-MPCP coated portions displayed an initial shear stress increase of ~0.1kPa during the first 50μm of motion, suggesting a static friction

contribution. Unlike the platinum coated region, sliding in the PDA-MPCA region did not increase stress past this initial rise, suggesting that interaction with unwetted portions of the probe did not increase shear stress, perhaps due to an existing bound water layer.
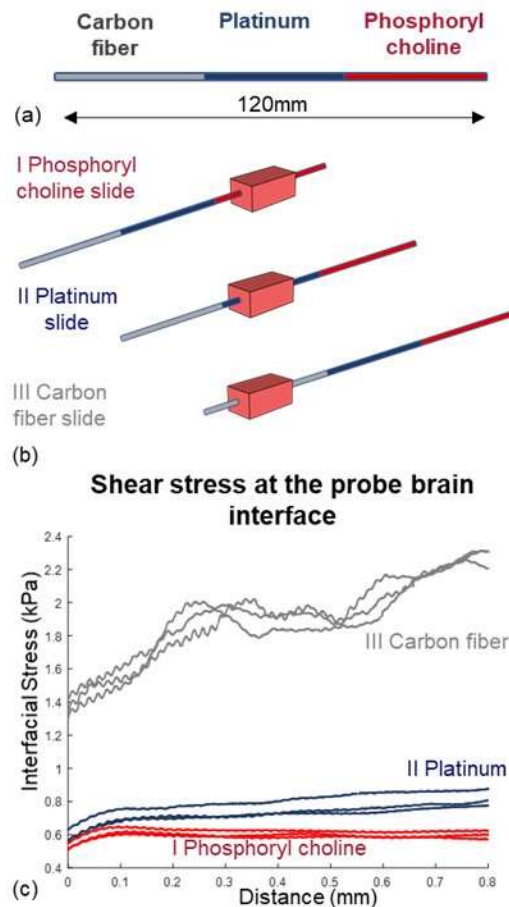
Figure 5.5. Demonstrating friction reduction with the PDA-MPCP coating. A) Schematic of the carbon fiber rod utilized in these experiments, containing an uncoated carbon fiber surface, a platinum coated surface, and PDA-PMPC coated surface. B) Schematic demonstrating the lamb brain sliding against the three variously coated portions of the rod following insertion. C) Interfacial shear stress calculated based on the PDA-PMCP, platinum, and carbon fiber portions of the rod interacting with the lamb brain.

Validation through surgical simulation

Tissue model selection: Post-mortem porcine brain confined within the skull was selected for testing during surgical simulations. Porcine tissue was selected due to comparable brain mass to rhesus monkeys (~10^2 g), which enables probe insertion to the 30mm depth targeted for primate studies.[92,93] Confinement within the skull was preferred over isolated brain tissue because confinement effects have previously been shown to create stiffening artifacts for penetration depths of 4mm.[94] The presence of the skull also allowed for representative placement of the insertion guide. Further, probing porcine brain <24h post mortem is representative of live tissue neural probe insertion conditions. The mechanical properties of hydrated brain tissue within five days post-mortem do not deviate significantly unless continuous mechanical perturbation is applied, with white and grey matter moduli remaining within 5% of original values.[95] Specifically in porcine brains, in-vivo perfusion through vasculature affects only the long-term time constant of relaxation.[94]

Surgical implementation: The probe delivery device design was validated through a porcine head tissue surgical simulation. As illustrated schematically in **Figure 5.6a**, grid insertion guide was mounted to the exposed skull of a porcine head directly over exposed brain tissue. A probe was inserted through the insertion guide and imaged via MRI. **Figure 5.6b** displays the porcine head and insertion guide in alignment with the load cell during probe insertion. The load displacement curves obtained from coated probe insertion during these experiments display three distinct regions: i) a rapid load increase characteristic of initial tissue penetration, ii) continuous insertion through the brain tissue, and iii) rapid load increase indicating collision with the skull (**Figure 5.6c**). Subsequent MRI imaging confirms the collision interpretation of the load increase: a sagittal view cross-section demonstrates the tip of the probe at the skull surface, confirming probe insertion through the whole tissue sample (**Figure 5.6d**). Probe deflection relative to the path projected based on insertion guide position was not calculated, as insertion of multiple probes into the sample combined with insufficient imaging resolution to define complete probe paths rendered analysis unreliable.
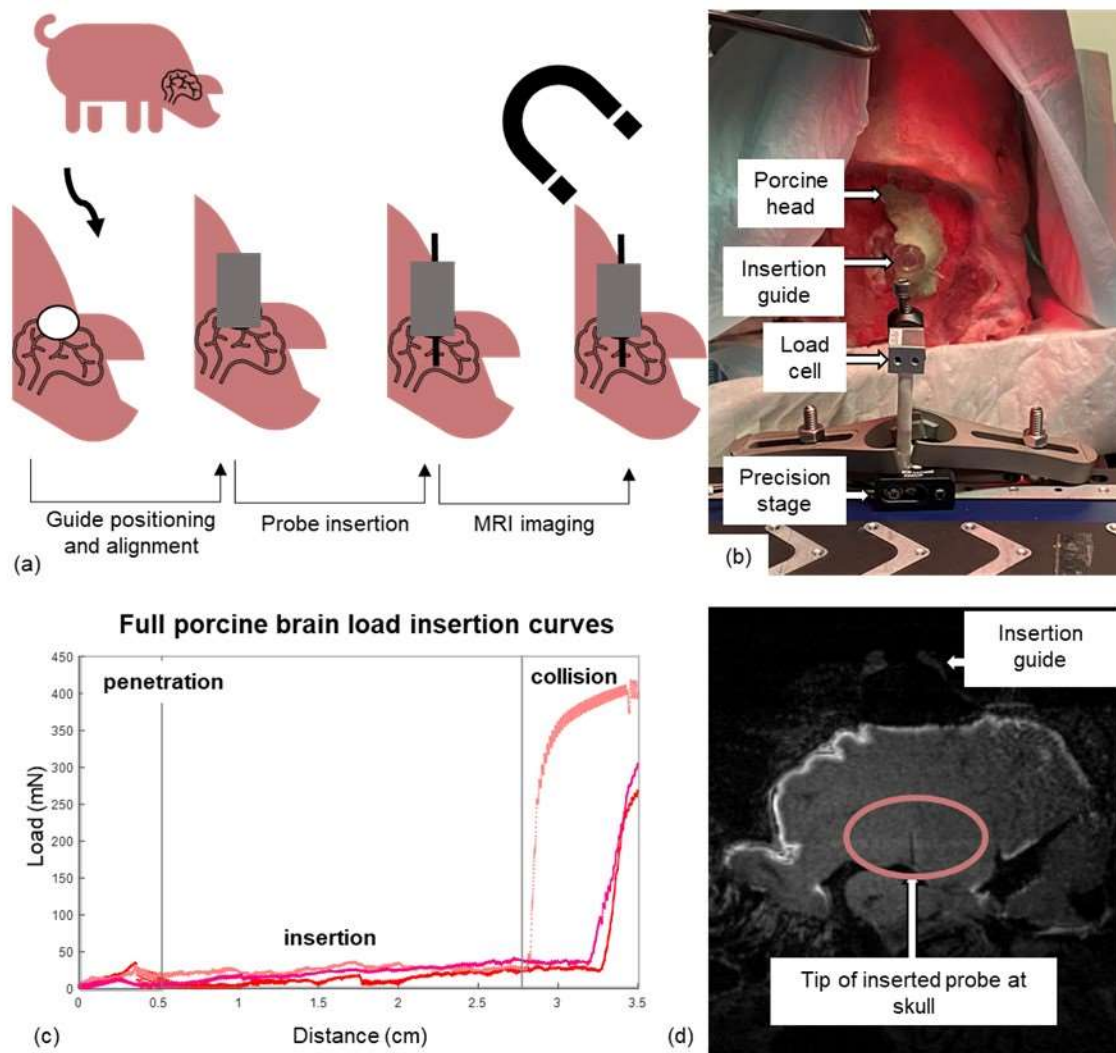
Figure 5.6. Surgical demonstration of probe insertion into porcine brain. A) Schematic of the porcine probe insertion simulation, including insertion guide grid positioning, probe insertion, and MRI imaging. B) Experimental setup for the porcine probe insertion. C) Load displacement curves for coated probe insertion, demonstrating the loading during initial brain penetration, insertion, and collision with the skull. N=3 D) MRI imaging slice from the sagittal view, highlighting the tip of the probe in contact with the skull.

5.5 Summary and outlook

Lamb brain insertion experiments performed using a carbon fiber based platinum coated probes indicate that friction plays a significant role in deep brain neural probe delivery,

accounting for 59 +/- 3% of work during a 3cm insertion. Friction was reduced through the facile application of a phosphorylcholine-based coating, resulting in a 20 +/- 7% reduction in shear stress at the brain-probe interface. The usability of these probes under conditions imitating primate probe placement surgeries was verified through a porcine head model, resulting in insertion through the whole tissue samples as confirmed by load monitoring and MRI imaging that indicate collision with skull at the opposing side of the brain. These experiments indicate that maximum loading during large brain neural probe insertions can be reduced by minimizing the contribution of friction.

The application of low friction coatings to deep brain insertion devices can expand the range of materials and geometries suitable for implantation. Unlike existing surface stiffness reducing hydrogel coatings, these nanoscale materials do not significantly impact probe cross-sectional areas, and therefore are not expected to result in increased foreign body response.[96] Indeed, the decrease in required critical buckling load for successful insertions will expand the array of viable foreign body response minimizing materials and geometries applicable to recording within large scale brains, perhaps including electrodes directly based on carbon fibers.

The particular carbon fiber and phosphorylcholine probe utilized in this study is a suitable deep brain delivery vehicle for flexible probes such as the proposed architected shape memory devices. The targeting device represents an improvement in density (7.85 g/cm^3 vs 15.2 g/cm^3) and footprint (0.06 mm^2 vs 0.09 mm^2) over the existing commercial alternative, and the predicted critical buckling load (108mN) is above the maximum loading observed during porcine insertion simulations prior to skull collision (48mN). The 84mm length of the device is compatible with existing probe positioning guide systems and visualization through MRI is possible, although resolution is reduced in our experiments due to post-mortem increases in tissue T1 relaxation time.[97]

5.6 Experimental methods

Probe fabrication

A 280µm diameter unidirectional carbon fiber rod (E= 131GPa, RockWest composites) was cut into 84mm components unless otherwise noted. Probes were coated with 10nm platinum with a high resolution sputter coater (Cressington). The probes were plasma activated for 10 minutes under oxygen flow in a plasma asher (Zepto B, Diener electronic). Coating solution was prepared by dissolving dopamine hydrochloride (10mg, 0.065 mmol) and 2-methacryloyloxyethyl phosphorylcholine (150mg, 0.51 mmol) in Tris buffer solution (5 ml, 10mM, pH=8.5). Aliquots of the solution were drawn into 1ml syringes and plasma activated coated probes were immersed for 24 hours at room temperature under shaking conditions. The probes were then rinsed and stored in phosphate buffer saline.

Probe characterization

Raman spectroscopy: Raman data were collected for platinum coated as well as platinum and PDA-MPCP coated glass slides using a Renishaw M1000 Raman Spectrometer system under 514 nm incident laser radiation. Ten accumulations at 10 seconds each were obtained. Spectra were baseline corrected and smoothed.

Probe insertion

Insertion guide grid: A modified version of the insertion grid typically used in primate surgeries for magnetic resonance guided stereotactic navigation of electrophysiology probes was printed from PR 48 in the Ember 3D printer (Autodeck). The grid design was obtained from a public repository containing the implantation planning software (https://github.com/shayo/Planner) and modified to limit the number of perpendicular guide holes to 4 with 700µm diameters. Soft rubber tubing with 636µm outer diameter and 300µm inner diameter (51845K65, McMaster Carr) was mounted into the grid hole with colloidal graphite.

Tissue container: A tissue container was printed from PR48 resists on the Ember 3D printer (Autodeck). The container was 25mm wide and 75mm long with a base, a solid wall on one side, a wall with an opening for insertion guide grid mounting, and a corner support to facilitate glass slide window mounting. The end of the container directly opposite the insertion guide mount position was open with a ridge at the base to avoid liquid leakage. The glass slide window was mounted with superglue and the insertion guide grid was mounted to a ridge from the outside of the container with carbon paste. The container was mounted on a manual linear stage positioned on an elevated optical breadboard plate. Tissue containers were disposed of after single day use.

Lamb tissue preparation: Individually packaged frozen lamb brains were thawed for 3 hours in phosphate buffer saline to room temperature. An individual lobe was excised from the remainder of the brain with a razorblade and the dura was pealed off, exposing the frontal lobe for probe insertion. The lobe was placed in the tissue container with the frontal lobe facing the insertion guide.

Porcine tissue preparation: A fresh porcine head specimen was prepared by Sierra for Medical Science (Whittier, CA). The top of the head was removed to expose the surface of the brain. The insertion guide grid was mounted to the skull with bone cement (Palacos$^{®}$ R, Heraeus). The head was secured with a stereotactic frame (900A, David Kopf Instruments) such that the opening in the skull was directly opposite the load cell.

Displacement controlled insertion: A resistive single point aluminum load cell with 100g capacity and maximum non-linearity of 0.05% with a USB interface (Loadstar Sensors) was mounted to a set of two precision linear stages (V-551.7B, PhysikInstrumente) with a 2-axis motion controller (A-812.21B00 ACS SPiiPlus, ACS Motion Control). Loading data was sampled at 1KHz and recorded through the LoadVUE Pro software (Loadstar Sensors). Displacements of 3cm to 7cm were programmed through the SPiiPlus ADK Suite V2.70 software (ACS motion control) at 10mm/s velocity, 1000 mm/s^2 acceleration, and 5000 mm/s^3 jerk. The tested probe was mounted to the load cell through 3D printed cylindrical

adapter with 300μm holes at 1mm depth via colloidal graphite. The entire system was located on an optical table.

MRI Imaging

Vaseline was applied as contrast to the outside perimeter of the insertion guide grid. Gadolinium contrast agent was flown into the insertion guide holes. The porcine head was scanned in a Siemens 3T Tim Trio. Anatomical scans were acquired with the T1w protocol using the following parameters: TR= 2300 ms, TE=3.17 ms, FOV= 128, TI=1100, flip angle = 8, slice thickness: 0.5mm, in-slice resolution: 0.5mm. Three sequential scans were averaged for analysis.

Chapter 6

SUMMARY AND OUTLOOK

6.1 Summary

In this thesis, we explored glass-transition based 3D micro-architected shape memory polymers with the goal of enabling complex stimuli responsive devices for microscale applications. We started by developing a two-photon lithography-based approach to fabricating these shape memory materials. We designed a polymer network incorporating monofunctional acrylate monomers and achieved a range of architectures with sub-micron feature sizes previously inaccessible for shape memory materials at this scale. We then characterized the expected glass transition-based shape memory mechanism of these materials by probing their viscoelastic properties as a function of temperature in uniaxial compression based dynamic nanomechanical analysis experiments. We observed the initiation of a glass transition region at 60°C not present in standard highly crosslinked two-photon lithography materials, indicating that the designed network incorporated flexible chains with temperature dependent mobility. We also demonstrated the tunability of the observed response through controlling network characteristics via fabrication parameters. Based on the obtained glass transition characteristics, we quantified the shape memory response in individual architected shape memory structures, observing *in-situ* programming cycles with a recovery ratio of 86 +/-4 % typical of macroscale materials. We have therefore enabled the design of architected shape memory structures on the micron scale.

We then focused on a particular potential application for these materials: deep brain neural probe delivery at the centimeter scale. We recognized high loading requirements incompatible with buckling-free insertion of microscale polymer-based probes as a key obstacle to deploying shape memory materials at the target depth. Through lamb brain tissue experiments, we identified friction as a key contributor to probe insertion loading,

and minimized it *via* a phosphorylcholine-based nanoscale coating applied to carbon fiber probes. We validated the insertion of these devices to the target 3cm depth in porcine surgical model, thereby demonstrating a potential delivery vehicle for architected microscale electrodes.

6.2 Shape memory neural probe device integration

The developed class of architected shape memory materials can be integrated with the designed deep brain delivery platform to produce a long-term neural monitoring device for application in large-scale brains. Specifically, we envision a shape memory lattice with pore geometry and sizes optimized for long term interaction with neural tissue through cell culture studies tuned to deploy at neural migration rates (~1µm/min) following plasticization at 6 hours post-surgical implantation. Tunability in the shape memory response can be achieved through composition and degree of crosslinking adjustments in a biocompatible shape memory polymer system based on photopolymerizable components, such as tert-butyl acrylate (tBA) and polyethylene glycol diacrylate (PEGDA).

The lattice would be mounted to a carbon fiber probe, which can be coated with nanoscale friction reducing coating and further miniaturized to the minimum diameter necessary for reliable implantation at < 2° deviation from targets 3cm within the brain (**Figure 6.1a**). Programming the lattice through compression would convert it to the stiff configuration utilized during delivery to the monitoring region (**Figure 6.1b-c**). The deployment distance post implantation would be tuned such that electrodes are positioned outside of the encapsulation and dead zone surrounding the carbon fiber insertion vehicle and detectable by histology studies (**Figure 6.1d-e**). This two-stage coarse and microscale positioning approach would enable accurate deep brain positioning while achieving desirable low stiffness and density characteristics at the recording site.

The electrode design described above focuses on the mechanical issues associated with successful implantation. As such, it could serve exclusively as a delivery tool, positioning

an independent flexible polymer electrode such as the polyimide-based devise designed for silicon shuttle delivery by Felix *et al.*.[98] Future development could focus on integrating electrode functionality directly into the shape memory component of the device to minimize the total footprint. This will introduce additional material requirements: efficient adhesion to gold leads through functional groups such as thiols,[83] minimal swelling,[83] hydrolytic stability,[99] high temperature tolerance necessary for micro-fabrication processes and compatibility with electrically insulating barrier layers.[100]

Deployments of this probe design for application in primate subjects would require thorough validation of biocompatibility. General material biocompatibility can be assessed *in-vitro* via polymer leaching studies and cell culture experiments with immortalized fibroblast, microglia cell lines as well as CNS neural primary cells.[101] To assess glial scar formation specifically, a model incorporating a mixture of glial and neuronal cultures could be utilized.[102] Initial *in-vivo* studies would involve subcutaneous implantation in porcine models to evaluate potential systemic toxicity.[103] Neurological foreign body response following implantation can then be characterized through standard histological staining and immunohistochemistry of excised mouse brain tissue by determining the position of neurons and identifying inflammation response markers such as reactive astrocytes, activated microglia and glial scar formation.[20]
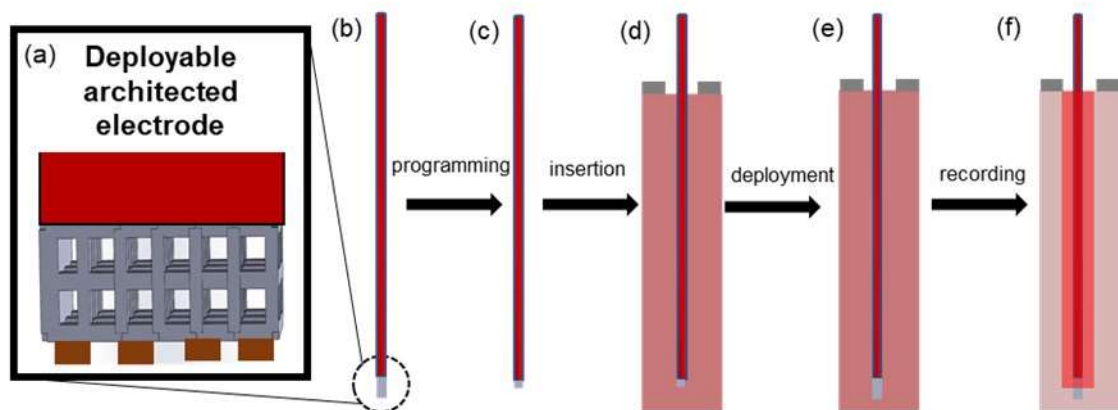

Figure 6.1. Schematic of two-stage deployment electrode design for deep brain neural recording. a) Architected microscale shape memory electrode deployment device for neural

electrodes. b) Positioning of shape memory component at the tip of a centimeter-scale carbon fiber based delivery device for deep brain coarse positioning. c) Shape memory electrode programming through compression to prepare for in-vivo deployment. d) Surgical positioning of the combined device within the brain. e) Post-surgical deployment of the shape memory component. f) Neural recording outside of the zone immediately surrounding the carbon fiber initial positioning device to avoid tissue affected by dead zones and encapsulation represented in red. Not drawn to scale.

6.3 Scalable fabrication

The architected shape memory system explored in this thesis relies on a highly flexible but low through-put microfabrication method of two-photon lithography. Currently under development as a collaboration between the Greer and Faron labs,is a more scalable interference lithography-based method of fabricating architectures with sub-micron features. This method relies on a metasurface mask that generates complex 3D light intensity distributions within a photoactive resist (**Figure 6.2**).[104] Laser scanning and automated tiling can currently be used to generate patterns with up to a $12cm^2$ footprint at volumetric throughput of $0.16mm^3$/min, which, when compared to the fabrication method described in this thesis, is at least a five orders of magnitude improvement in throughput and a four orders of magnitude increase in maximum footprint achievable at that speed.

Although the metasurface-based fabrication approach cannot generate arbitrary 3D patterns, control light phase, intensity, and polarization afforded by the metasurfaces could be used to fabricate a variety of exotic patterns, such as gyroids, diamonds, or cubes, that are currently inaccessible through mutli-laser or phase mask interference approaches.[95] Given that we have so far described an effective glass transition based shape memory response for structures with sub-micron features, developing shape memory materials compatible with this fabrication method can produce microscale responsive architectures at the scale necessary for commercial applications. For instance, we envision the rapid fabrication of arrays of spirals for clot retrieval in retinal vein occlusion and large-scale sheets with stimulus activated mechanic cloaking properties.
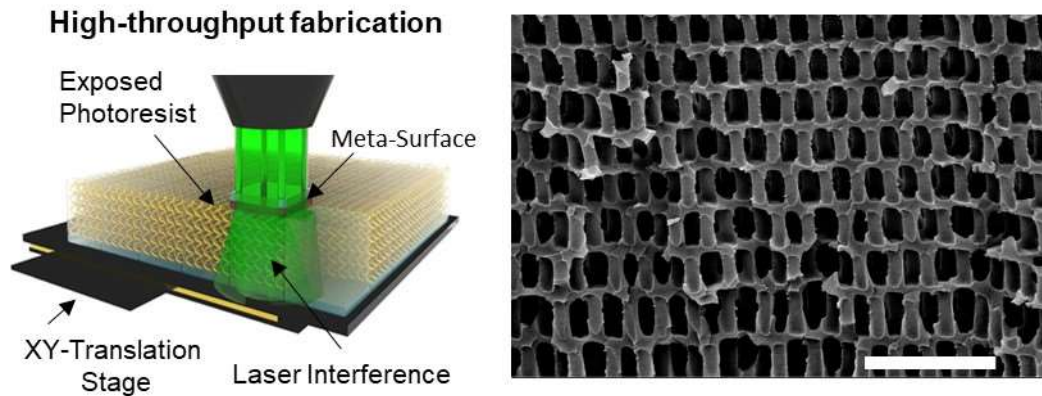
Figure 6.2. A metasurface-based scalable approach to micro-architected material fabrication. (a) A schematic illustrating single laser metasurface-based interference lithography, demonstrating exposure of a single region and the x-y stage utilized to achieve increased footprints through tiling. Not drawn to scale. Courtesy of Mahsa Kamali. (b) SEM image of the cross section of a lattice fabricated through metasurface based interference lithography. Scale bar 5 μm. Image courtesy of Andrew Friedman.

BIBLIOGRAPHY

[1] B. Q. Y. Chan, Z. W. K. Low, S. J. W. Heng, S. Y. Chan, C. Owh, X. J. Loh, *ACS Appl. Mater. Interfaces* **2016**, *8*, 10070.

[2] A. Lendlein, O. E. C. Gould, *Nat. Rev. Mater.* **2019**, *4*, 116.

[3] Q. Ge, A. H. Sakhaei, H. Lee, C. K. Dunn, N. X. Fang, M. L. Dunn, *Sci. Rep.* **2016**, *6*, 1.

[4] V. Srivastava, S. A. Chester, L. Anand, *J. Mech. Phys. Solids* **2010**, *58*, 1100.

[5] C. Lin, L. J. Zhang, Y. J. Liu, L. W. Liu, J. S. Leng, *Sci. China Technol. Sci.* **2020,** *63*, 578.

[6] M. Zarek, N. Mansour, S. Shapira, D. Cohn, *Macromol. Rapid Commun.* **2016**, *38,* 1600628.

[7] M. Zarek, M. Layani, I. Cooperstein, E. Sachyani, D. Cohn; S. Magdassi, *Adv. Mater.* **2016**, *28*, 4449.

[8] X. Wu, W. M. Huang, Y. Zhao, Z. Ding, C. Tang, J. Zhang, *Polymer* **2013**, *5,* 1169.

[9] M. Deb-Chatterji, A. Konnopka, F. Flottmann, H. Leischner, J. Fiehler, C. Gerloff, G. Thomalla, *Neurology* **2020***, 95,* e1724.

[10] A. Alshekhlee, D. J. Pandya, J. English, O. O. Zaidat, N. Mueller, R. Gupta, R. G. Nogueira, *Neurology* **2012**, *79*, S126.

[11] S. Rohde, J. Bosel, W. Hacke, M. Bendszus, *J. Neurointerv. Surg.* **2012**, *4,* 455.

[12] A. T. Raj, J. P. Hogg, B. Cline, G. Hobbs, *J. Neuroimaging* **2013***, 5,* 371.

[13] P. Widimsky, L. N. Hopkins, *Eur. Heart J.* **2016**, *37,* 3081.

[14] M. Ho, D. T. L. Liu, D. S. C. Lam, J. B. Jonas, *Retina* **2016***, 36,* 432.

[15] M. D. de Smet, T. C. M. Meenink, T. Janssens, V. Vanheukelom, G. J. L. Naus, M. J. Beelen, C. Meers, B. Johckx, J. M. Stassen, *PLOS ONE* **2016***, 11,* e0162037.

[16] J. Bauer, S. Hengesbach, I. Tesari, R. Schwaiger, O. Kraft, *PNAS* **2014***, 111*, 2453.

[17] W. P. Moestopo, A. J. Mateos, R. M. Fuller, J. R. Greer, C. M. Portela, *Adv. Sci.* **2020***, 7,* 2070115.

[18]   T. Frenzel, M. Kadic, M. Wegener, *Science* **2017***, 358,* 1072.

[19]   T. Buckmann, M. Thiel, M. Kadic, R. Schittny, M. Wegener, *Nat. Commun* **2014**, *5,* 4130.

[20]   G. Kook, S. W. Lee, H. C. Lee, I. J. Cho, H, J. Lee, *Micromachines* **2016***, 7,* 179.

[21]   A. Campbell, C. Wu, *Micromachines* **2018***, 9,* 430.

[22]   A. A. Sharp, H. V. Panshawagh, A. Ortega, R. Artale, S. Richardson-Burns, D. S. Finch, K. Gall, R. L. Mahajan, D. Restrepo, *J. Neural Eng.* **2006**, *3,* L23.

[23]   G. D. Mahumane, P. Kumar, L. C. du Toit, Y. E. Choonara, V. Pillay, *Biomater. Sci.* **2018***, 6,* 2812.

[24] W. Kuhn, *Naturwissenschaften* **1936**, *24*, 346.

[25] S. F. Edwards, *Proc. Phys. Soc.* **1967**, *92*, 9.

[26] F. Di Lorenzo, J. Hellwig, R. von Klitzing, S. Seiffert, *ACS Macro Lett.* **2015**, *4* , 698.

[27] F. D. Lorenzo, S. Seiffert, *Polym. Chem.* **2015**, *6*, 5515.

[28] S. Reddy, E. Arzt, A. del Campo, *Adv. Mater.* **2007**, *19*, 3833.

[29]   J. D. Eisenhaure, T. Xie, S. Varghese, S. Kim, *ACS Appl. Mater. Interfaces* **2013**, *5*, 7714.

[30] H, Xu, C. Yu, S. Wang, V. Malyarchuk, T. Xie, J. A. Rogers, *Adv. Funct. Mater.* **2013**, *23*, 3299.

[31] C.-M. Chen, S. Yang, *Adv, Mater.* **2014**, *26*, 1283.

[32] M. Ebara, K. Uto, N. Idota, J. M. Hoffman, T. Aoyagi, *Soft Matter* **2013**, *9,* 3074.

[33] W, Li, T. Gong, H. Chen, L. Wang, J. Li, S. Zhou, *RSC Adv.* **2013**, *3*, 9865.

[34] M. Ebara, K. Uto, N. Idota, J. M. Hoffman, T. Aoyagi, *Adv. Mater*. **2012**, *24*, 273.

[35] W. Niu, L. Qu, R. Lyv, S. Zhang, *RSC Adv.* **2017**, *7*, 22461.

[36] C. Wischke, M. Schossig, A. Lendlein, *Small* **2014**, *10,* 83.

[37] Y. Liu, M. Y. Razzaq, T. Rudolph, L. Fang, K. Kratz, A. Lendlein, *Macromolecules* **2017**, *50,* 2518.

[38] S. M. Brosnan, A.-M. S. Jackson, Y. Wang, V. S. Ashby, *Macromol. Rapid Commun*. **2014**, *35,* 1653.

[39] I. Apsite, A. Biswa, Y. Li, L. Ionov, *Adv. Funct. Mater*., **2020**, *30*, 1908028.

[40] C. de Marco, C. C. J. Alcantara, K. Sangwon, F. Briatico, A. Kadioglu, G. de Bernardis, X. Chen, C. Marano, B. J. Nelson, S. Pane, *Adv. Mater. Technol*., **2019**, 4, 1900332.

[41] X. Zhou, Y. Hou, J. Lin, *AIP Advances* **2015**, *5,* 030701.

[42] L. J. Jiang, Y. S. Zhou, W. Xiong, Y. Gao, X. Huang, L. Jiang, T. Baldracchini, J. F. Silvani, Y. F. Lu, *Opt. Lett.* **2014**, *39,* 3034.

[43] I. S. Ladner, M. A. Cullinan , S. K. Saha, *RSC Advances,* **2019**, *9*, 28808.

[44] J. B. Mueller, J. Fischer, Y. J. Mange, T. Nann, M. Wegener, *Appl. Phys. Lett.* **2013**, *103*, 123107.

[45] D. L. Safranski, K. Gall, *Polymer* **2008**, *49*,446.

[46] J. B. Muller, J. Fischer, Y. J. Mange, T. Nann, M. Wegner, *Appl. Phys. Lett.* **2013***, 103,* 123107.

[47] M. R. Belegratis, V. Schmidt, *Laser Technology in Biomimetics: Basics and Applications,* Springer Berlin Heidelberg, **2014***,* 24.

[48] S. E. Barnes, Z. T. Cygan, Z. T., J. K. Yates, K. L. Beers, E. J. Amis, *Analyst* **2006**, *131*, 1027.

[49] G. Socrates, *Infrared and Raman Characteristic Group Frequencies: Tables and Charts*, John Wiley & Sons, **2004**.

[50] L. Lay, M. R. Lee, H. K. Lee, I. Y. Phang, X. Y. Ling, *ACS Nano* **2015**, *9*, 9708.

[51] Y.-L. Zhang, Y. Tian, H. Wang, Z.-C. Ma, D.-D. Han, L.-G. Niu, Q.-D. Chen, H.-B. Sun, *ACS Nano* **2019**, *13*, 4041.

[52] J. W. Chan, C. E. Hoyle, A. B. Lowe, M. Bowman, *Macromolecules* **2010**, *43*, 6381.

[53] D. W. Yee, M. D. Schulz, R. H. Grubbs, J. R. Greer, *Adv. Mater.* **2017**, *29*, 1605293.

[54] S. Noel, B. Liberelle, L. Robitaille, G. De Crescenzo, *Bioconjugate Chem.* **2011**, *22*, 1690.

[55] K. M. Ainslie, R. D. Lowe, T. T. Beaudette, L. Petty, E. M. Bachelder, T. A. Desai, *Small* **2009**, *5*, 2857

[56] H. Zhang, H. Xia, Y. Zhao, *J. Mater. Chem*. **2011**, *22*, 845.

[57] Y. F. Lu, Y. M. Wang, X. D. Chen, M. H. Miao, D. H. Zhang, *Express Polym. Lett*. **2020**, *14*, 192.

[58] S. Podzimsky, *Light Scattering, Size Exclusion Chromatography and Asymmetric Flow Field Flow Fractionation: Powerful Tools for the Characterization of Polymers, Proteins and Nanoparticles*, John Wiley & Sons, Inc, **2011**, Ch. 1.

[59] C. C. Hornat, Y. Yang, M. W. Urban, *Adv. Mater.* **2017**, *29*, 1603334.

[60] C. C. Hornat, M. Nijemeisland, M. Senardi, M. Senardi, Y. Yang, C. Pattyn, S. van der Zwaag, M. W. Urban, *Polymer* **2020***, 186,* 122006.

[61] S. A. Hayes, A. A. Goruppa, F. R. Jones, *J. Mater. Res*. **2004**, *19,* 3298.

[62] S. B. Hutchens, L. J. Hall, J. R. Greer, *Adv. Funct. Mater.* **2010**, *20*, 2338.

[63] E. G. Herbert, W. C. Oliver, G. M. Pharr*, J. Phys. D: Appl. Phys*. **2008**, *41*, 074021.

[64] W. J. Wright, W. D. Nix, *J. Mater. Res.* **2009**, *24*, 863.

[65] I. S. Ladner, M. A. Cullinan , S. K. Saha, *RSC Advances*, **2019**, *9*, 28808.

[66] C. M. Yakacki, R. Shandas, C. Lanning, B. Rech, A. Eckstein, K. Gall, *Biomaterials* **2009**, *28*, 2255.

[67] R. A. Orza, P. C, M. M. Magusin, V. M. Litvinov, M. van Duin, M. A. J. Michelts, *Macromolecules* **2007***, 40,* 8999.

[68] G. Li, A. Wang, *J. Polym. Sci. B Polym. Phys.* **2016**, *54,* 1319.

[69] L. Fang, O. E. C. Gould, L. Lysakova, Y. Jiang, T. Sauter, O. Frank, T. Becker, M. Schossig, K. Katz, A. Lendlein, *Chemphyschem* **2018,** *19,* 2078.

[70] M. Behl, J. Zotzmann, A. Lendlein, in *Shape Memory Polymers. Advances in Polymer* Science Vol. 226 (Eds: A. Lendlein), Springer, Berlin, Heidelberg **2010**, Ch. 1

[71] B. Li, X. Lu, Y. Ma, X. Han, Z. Chen, *ACS Macro Lett*. **2015**, *4*, 548.

[72] J. Rys, S. Steenhusen, C. Schumacher, C. Cronauer, C. Daraio, *Extreme Mech. Lett*. **2019**, *28*, 31.

[73] A. Bauhoufer, C. Daraio, *Int. J. Adv. Manuf. Technol.* **2020**, *107*, 2563.

[74] A. A. Bauhofer, S. Krodel, J. Rys, O. R. Bilal, A. Constantinescu, C. Daraio, *Adv. Mater.,* **2017**, *29,* 1703024.

[75] S. Ohayon, D. Tsao, *J. Neurosci. Methods.* **2012**, *204*, 389.

[76] J. E. Chung, H. R. Joo, J. L. Fang, D. F. Liu, A. H. Barnett, S. Chen, C. Greagham-Breiner, M. P. Karlsson, M. Karlsson, K. Y. Lee, H. Liang, J. F. Magland, J. A. Pebbles, A. C. Tooker, L. F. Greengard, V. M, Tolosa, L. M. Frank, *Neuron* **2019,** 1, 21.

[77] J. Jiang, E. Yin, C. Wang, M. Xu, D. Ming, *J. Neural Eng.* **2018***, 15,* 046025.

[78] D. H. Szaowski, M. D. Andersen, S. Retterer, A. J. Spence, M. Isaacson, H. G. Craighead, J. N. Turner, W. Shain, *Brain Res.* **2003***, 983,* 23.

[79] https://www.microprobes.com/products/multichannel-arrays/mba

[80] G. Lind, C. E. Linsmeier, J. Schouenborg, *Sci Rep* **2013**, *3*, 2942*.

[81] P. Singhal, A. Boyle, M. L. Brooks, S. Infanger, S. Letts, W. Small, D. J. Maitland, T. S. Wilson, *Macromol. Chem. Phys.* **2012***, 214,* 1204.

[82] E. H. Immergit, H. F. Frank in *Plastization and Plastisizer Processes*, *Principles of Plastization,* Am. Chem. Soc. **1965***,* Ch. 1.

[83] T. Ware, D. Simon, K. Hearon, T. H. Kang, D. J. Maitland, W. Voit, *Macromol. Biosci* **2013***, 13,* 1604.

[84] A. Obaid, Y. W. Wu, M. Hanna, W. Nix, J. Ding, N. Melosh, *bioRxiv*, 2018.

[85] L. N. Woodard, K. T. Kmetz, A. A. Roth, V. M. Page, M. A. Grunlan, *Biomacromolecules* **2017**, *18*, 4075.

[86] L. Ma, A. Gaisinskaya-Kipnis, N. Kampf, J. Klein, *Nat. Commun* **2015** *6,* 6060.

[87] K. Ishihara, *Polym J* **2015***, 47*, 585.

[88] F. Foglia, M. J. Lawrence, C. D. Lorenz, S. E. McLain, *J. Chem. Phys.* **2010***, 133,* 145103.

[89] Q. Wei, X. Liu, Q. Yue, S. Ma, F. Zhou, *Langmuir* **2019***,35,* 8068.

[90] J. Feng, H. Fan, D. Zha, L. Wang, Z. Jin, *Langmuir* **2016***, 32,* 10377.

[91] K. Filipecka, R. Miedzinski, M. Sitarz, J. Filipecki, M. Makowska-Janusik, *SAA* **2017**, 176, 83.

[92] M. S. Conrad, R. N. Dilinger, R. W. Johnson, *Dev. Neuroscie.* **2012***, 34,* 291.

[93] M. S. Franklin, G. W. Kraemer, S. E. Shelton, E. Baker, N. H. Kalin, H. Uno, *Brain Res.* **2000***, 852,* 263.

[94] A. Gefen, S. S. Margulies, *J. Biomech.* **2003,** *37,* 1339.

[95] S. Budday, R. Nay, R. de Rooij, P. Steinmann, T. Wyrobek, T. C. Ovaert, E. Kuhl, *J. Mech. Behav. Biomed. Mater.* **2015***, 46,* 318.

[96] K. C. Spencer, J. C. Sy, K B. Ramadi, A. M. Graybiel, R. Langer, M. J. Cima, *Scie. Rep.* **2017***, 7,* 1952.

[97] T. Kobayashi, S. Shiotani, K. Kaga, H. Saito, K. Saotome, K. Miyamoto, M. Kohno, K. Kikuchi, H. Hayakawa, K. Homma, *Jpn. J. Radiol.* **2010***, 28,* 8.

[98] S. Felix, K. Shah, D. George, V. Tolosa, A. Tooker, H. Sheth, T. Delima, S. Pannu, *Conf. Proc. IEEE Eng. Med. Biol. Soc.* **2012**, 871.

[99] S. M. Hosseini, R. Rihani, B. Batchelor, A. M. Stiller, J. J. Pancrazio, W. E. Voit, M. Ecker, *Front. Mater*. **2018,** *5***,** 66**.**

[100] C. J. Bettinger, M. Ecker, T. D. Y. Kozai, G. G. Malliaras, E. Meng, W. Voit, *MRS Bulletin* **2020**, *45*, 655.

[101] M. Gulino, D. Kim, S. Pane, S. D. Santos, A. P. Pego, *Front. Neurosci.* **2019***, 13,* 689.

[102] A. K. H. Achyuta, V. S. Polikov, A. J. White, H. G. Pryce Lewis, S. K. Murthy, *Macromol. Bioscie.* **2010**, *10,* 872.

[103] M. M. Swindle, A. Makin, A. J. Herron, F. J. Clubb, K. S. Frazier, *Vet. Pathol.* **2011**, *49,* 344.

[104] S. M. Kamali, E. Arbani, H. Kwon, A. Faraon, *PNAS* **2019***, 116,* 21379.

Appendix A

LEGEND OF SUPLEMENTAL VIDEOS

Supplemental Video 1

Shape memory recovery of a cubic lattice

Supplemental Video 2

Shape memory recovery of a pillar

Supplemental Video 3

Shape memory recovery of a flower

Supplemental Video 4

Shape memory recovery of a reduced crosslinking density pillar

Supplemental Video 5

Shape memory recovery of a reduced size pillar